National Laser Users' Facility and External Users' Programs

During FY05, 760 target shots were taken on OMEGA for external users' experiments. The external users' shots accounted for 52% of the total OMEGA shots produced in FY05. External users in FY05 included seven collaborative teams under the National Laser Users' Facility (NLUF) program as well as collaborations led by scientists from the Lawrence Livermore National Laboratory (LLNL), Los Alamos National Laboratory (LANL), Sandia National Laboratory (SNL), the Naval Research Laboratory (NRL), and the Commissariat à l'Énergie Atomique (CEA) of France.

NLUF Program

FY05 was the first of a two-year period of performance for the eight NLUF projects approved for FY05 funding. Seven of these NLUF campaigns were allotted OMEGA shot time and received 130 shots on OMEGA in FY05. Table 104.IV lists the accepted proposals.

Isentropic Compression Experiments (ICE) for Measuring EOS on OMEGA

Principal Investigator: J. R. Asay (Washington State University)

This research is developing three new areas of high-pressure research. First, techniques to generate high-accuracy, quasi-isentrope equation of state data into the Mbar regime will be developed. This effort will enable, for the first time using lasers, "cold" equation of state curves for standard materials in the Mbar regime. Second, wave profile data on candidate materials (Bi and Fe) upon compression through both solid–solid and solid–liquid phase transitions will be measured and compared with similar data measured with different loading times on other platforms (Z data, gun data, diamond anvil data). These data will then be used to benchmark models for the time dependence of phase transitions being developed at WSU. Finally, to ensure the phase transitions observed in these dynamic experiments correspond to the same phases as observed in

Table 104.IV: FY05–FY06 Proposals.

Principal Investigator	Affiliation	Proposed Title
J. Asay	Washington State University	Isentropic Compression Experiments for Measuring EOS on OMEGA
H. Baldis	University of California, Davis	Laser–Plasma Interactions in High-Energy-Density Plasmas
R. P. Drake	University of Michigan	Experimental Astrophysics on the OMEGA Laser
R. Falcone	University of California, Berkeley	NLUF Proposal: Plasmon Density of States in Dense Matter (no target shots allocated in FY05)
P. Hartigan	Rice University	Astrophysical Jets and HED Laboratory Astrophysics
R. Jeanloz	University of California, Berkeley	Recreating Planetary Core Conditions on OMEGA
R. Mancini	University of Nevada, Reno	Three-Dimensional Study of the Spatial Structure of Direct-Drive Implosion Cores on OMEGA
R. D. Petrasso and C. K. Li	Massachusetts Institute of Technology	Implosion Dynamics and Symmetry from Proton Imaging, Spectrometry, and Temporal Measurements

static experiments, dynamic x-ray diffraction will be used to determine lattice structure. This past year the most difficult of these goals were achieved; we developed the platform to produce high-accuracy and high-pressure isentrope data on aluminum. In addition, it was observed that the elastic–plastic transition is much larger than expected from previous work at Z. This issue is being investigated.

Twelve shots were performed on isentropic compression targets in the past year (Feb. 22th: shots 38961–38966, June 14th: shots 40121–40127). The purpose of these initial campaigns was to (1) develop a shockless compression platform with a pressure drive of ~1% planarity over a several hundred micron region and (2) use this planar drive to extract a single-shot series of equation of state (EOS) data for Al to peak pressures in excess of 1 Mbar. The ICE-EOS package, as shown in Fig. 104.58, consists of a Au halfraum, a plastic reservoir followed by a vacuum gap, and a double-stepped Al target. Fifteen beams from the OMEGA laser at 0.35-μm wavelength, containing a combined energy of 5–6 kJ in a 2-ns temporally flat pulse, are focused symmetrically onto the inner walls of the Au hohlraum laser entrance hole (LEH): 1.7-mm; diameter: 2.2 mm; length: 1.7 mm). This confined high-Z geometry results in a near blackbody distribution of thermal x rays (T_h ~ 120 eV) with uniform temperature gradients over a spatial region close to the diameter of the hohlraum. The hohlraum is attached to a 180-μm-thick, 12% Br-doped polystyrene foil [$C_8H_6Br_2$]. The x-ray field within the hohlraum launches an ablatively driven shock through the foil. The initial region of planarity is expected to approach that of the diameter of

the halfraum and can extend over millimeters. The Bromine dopant absorbs the high-energy Au M-band x rays generated within the hohlraum, which otherwise could preheat the Al step sample. After breakout from the rear surface, shock heating and momentum cause the Br-CH to dissociate and unload across a 400-μm vacuum gap. Transit across the vacuum gap causes mass-density gradients along the target axis to relax as a function of distance from the original Br-CH/vacuum-gap interface. The unloading Br-CH monotonically loads up against the Al sample and the imparted momentum launches a ramp stress wave through the material. The temporal profile of the compression wave may be shaped by varying the size of the vacuum gap, the density of the reservoir, or the temperature within the hohlraum. In our FY05 experiments, the main targets consisted of 10-20-30-μm Al steps coated onto a well impedence-matched LiF window.

Probing through the LiF window, the time history of the Al/LiF interface acceleration is recorded with a line imaging velocity interferometer (velocity interferometry system for any reflector or VISAR) with two channels set at different sensitivities. The time-resolved fringe movement recorded by a streak camera is linearly proportional to the velocity of the reflecting surface, which in this case is the Al-LiF interface. This allows for accurate measurement of the particle velocity (after taking into account the refractive index of the LiF window) as a function of time. Shown in Fig. 104.59(a) is the streak camera output of the VISAR for the target conditions described in Fig. 104.58.

The image provides spatial resolution at the target plane over ~500 μm and temporal resolution of the interferometer fringe displacement over a 30-ns time window. We observe excellent planarity across the field of view with smooth ramp unloading from the 10-, 20-, and 30-μm Al samples at progressively later times. The velocity sensitivity (set by the resolving element within the VISAR) is 0.86 km/s/fringe shift. Using Fourier analysis, and after deconvolving the data for temporal and spatial distortions within the streak camera, the time-resolved particle velocity profile for each Al thickness [Fig. 104.59(b)] can be extracted.

The iterative analysis technique described by Rothman et al.[1] was used along with the particle velocity profiles in Fig. 104.59(b) to generate a path through stress-density space (Fig. 104.60). Also shown for comparison is the isentrope from the Mie–Grüneisen equation of state. The error bars on the experimentally determined σ–ρ curve are ±5% (stress space) and ±2.5% (density space) up to a peak stress of ~83 GPa.

180-μm 12% Br-CH

10/20/30 μm Al

LiF window

15 beams
5.9 kJ, 2 ns

~2.26 mm

2-channel line VISAR

Au halfraum with
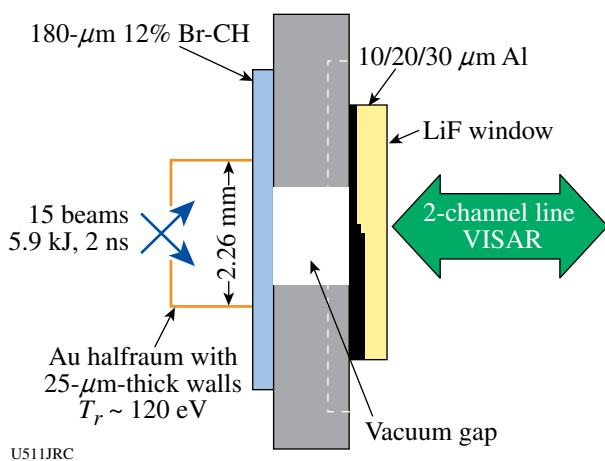25-μm-thick walls
T_r ~ 120 eV

Vacuum gap

U511JRC

Figure 104.58
Standard ICE target design.

The errors are dominated by uncertainties in measuring of the (~0.1 km/s), time (~50 ps), step height (~1%), and initial density (0.6%) and are due to random noise within the system (poor fringe visibility). The error bars can be reduced linearly with increasing step height. This is the first such measurement on a laser platform and opens up the possibility of extracting EOS data well into the multi-Mbar regime. Note that the extracted stress-density path is stiffer than the predicted Al isentrope, which may be due to strength effects or potential systematic errors in the experiment.

Shockless compression was demonstrated over a range of peak pressures and rise times (Fig. 104.61). The highest achieved pressure was 210 GPa, which corresponds to a particle velocity of ~6 km/s. An enhanced elastic wave precursor was observed, several times in excess of the reported Hugoniot elastic limit (HEL), for ramp compressions which occur over shorter time scales. This is not presently understood and is being investigated. If true, this is a significant discovery and it is expected that it will highlight the uniqueness of laser-driven ramp loading for measuring the yield strength of materials at high shockless strain rates. In the second year of the proposal,
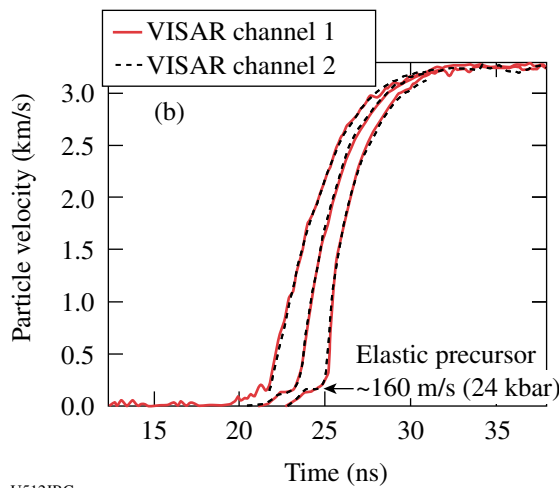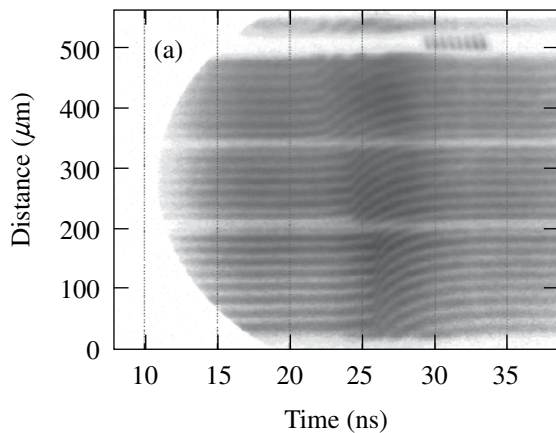

Figure 104.60
Stress-density path calculated from a double-stepped Al target.

Figure 104.59
(a) Streak camera output of VISAR for shot 40127. (b) Extracted particle velocity profiles for shot 40127.

Figure 104.61
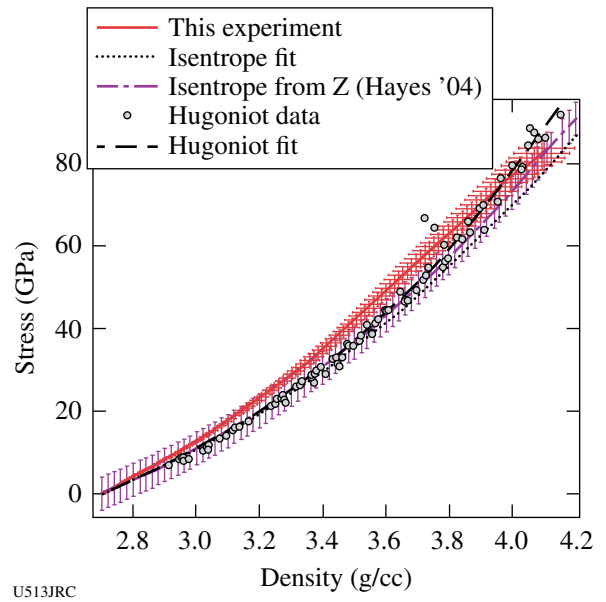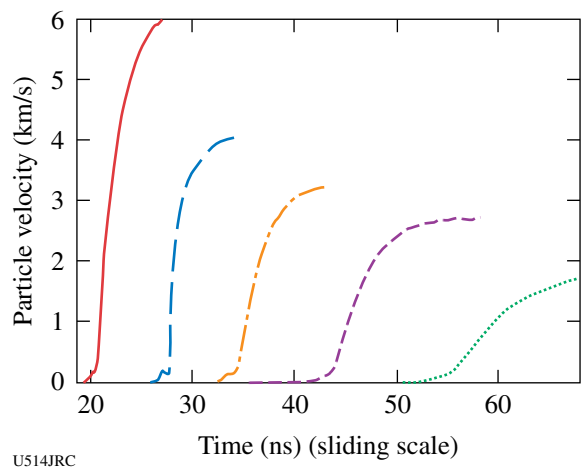The compression of Al samples for different compression times shows a difference in the elastic-plastic structure with loading rate.

it is intended to extract EOS and strength information for free-surface Ta in excess of 1 Mbar and to determine the rate dependence of phase transformations for materials with multiple solid phases. A sophisticated analysis technique is also being developed to analyze free-surface stepped data so that a window material is not needed as a reference. Some effort will also be dedicated to develop techniques to shape the pressure profile of the compression wave.

Laser–Plasma Interactions in High-Energy-Density Plasmas
Principal Investigator: H. Baldis (University of California, Davis)

Laser–plasma interactions in high-energy-density plasmas display a broad palette of features that prove useful in furthering the understanding and characterization of these unexplored plasma regimes. To access these regimes, reduced-size (below 1 mm in diameter and length), Au cylindrical enclosures are irradiated by intense laser beams at around 10-TW power in 1 ns. These hot hohlraums act as converters of laser energy into x-radiation, and because of the high power pumped into such a small target, the radiation temperature reaches high values, above 300 eV. The plasmas created into and around the laser channels are characterized by elevated electron temperatures (~10 keV), with densities varying up to the critical density (for 351 nm $n_{cr} = 9.1 \times 10^{20}$ cm^{-3}).

The intrinsic dependence of the stimulated Raman scattering (SRS) on plasma temperature and density gives the possibility of using the process as a plasma diagnostic tool. From the resonance condition coupled to the dispersion relation, one can infer the electron temperature in hot plasmas (above 5 keV) as the Bohm–Gross shift becomes significant and SRS wavelengths extend beyond 702 nm (= $2\lambda_0$, where λ_0 is the laser wavelength). The hot hohlraum is irradiated by 19 OMEGA laser beams. Each beam carries ~500 J energy onto the target, in 1 ns pulses, at 351-nm wavelength. The beams are bundled in cones at ~23° (cone 1), ~48° (cone 2), and 59° to 62° (cone 3) as shown in Fig. 104.62.

Figure 104.63 illustrates a SRS spectrum measured by a full-aperture backscattering station (FABS) at OMEGA. The SRS wavelength rises quickly in the first half of the laser pulse, as the laser channel fills with plasma. The electron density
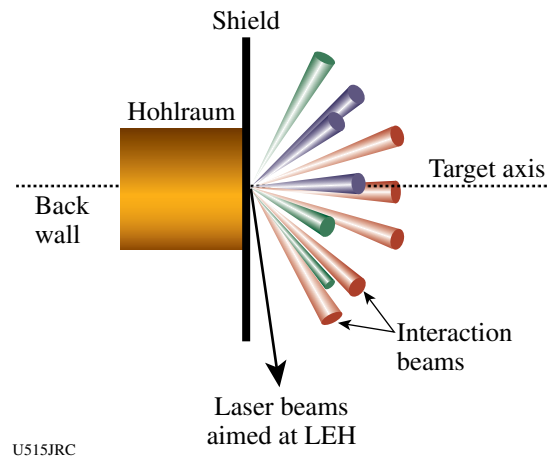

U515JRC

Figure 104.62
Hohlraums irradiated by the OMEGA beams are used for new studies of laser–plasma interaction in high-energy density plasmas.
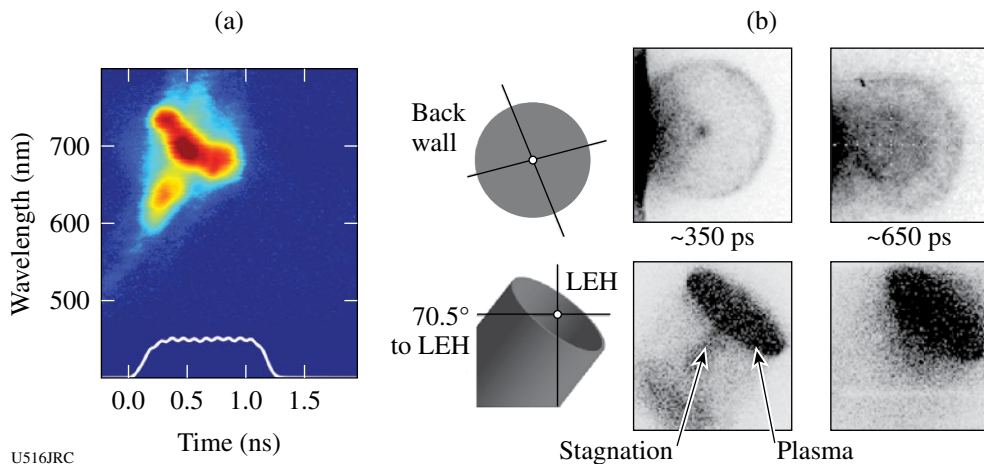

U516JRC

Figure 104.63
(a) A time-resolved Raman spectrum measured in hot hohlraums is characterized by a wavelength above 702 nm. This is an indication of high electron temperatures. (b) Two different views (end-on and near side-on) of the Au plasma-emitting x-rays with photon energies above 7 keV. The stagnation on axis is visible at 350 ps, with the bright emission at the LEH.

increases above 0.1 n_{cr}, and the plasma fill moves the laser energy deposition region to the laser entrance hole (LEH). Indications of plasma filling are given by the Raman spectra at the time when the SRS wavelength reaches its maximum and then stays constant or decreases. It is likely that SRS, occurring along a density gradient outside the target, is pushed to a lower density (shorter wavelength) as the laser beam filaments.

X-ray framing-camera images [Fig. 104.63(b)] confirm the filling time inferred from SRS spectra. The images were taken for x-ray photon energies above 7 keV, through the thin Au back wall of the hohlraum and also at 70.5° to the LEH. The Au plasma stagnation may be important for the scattering as it produces high electron temperatures ($T_e \sim 10$ keV). The stagnated plasma eventually moves to the LEH where it is further heated by the laser. This is reflected in the spectral shift that brings the SRS wavelength above 730 nm, which corresponds to $T_e \sim 8$ keV (as deduced from SRS dispersion relation). Time-integrated spectroscopic measurements of a Au L-band measured an average charge state of around 58 to 59, consistent with an average $T_e \sim 7$ to 8 keV.

Experimental Astrophysics on the OMEGA Laser
Principal Investigator: R. P. Drake (University of Michigan)

The OMEGA laser can address important issues in astrophysics because, through laser ablation, it can produce pressures of >>l0 Mbars over areas of square millimeters. Two such issues, the contribution of hydrodynamic instabilities to the structure in supernovae and the dynamics of radiative shock waves, are the topics of this project. In experiments performed in this project, it was found that, under conditions well scaled to supernova explosions, spikes of dense material can penetrate much farther than previously anticipated. To explore this phenomenon, it was necessary to develop new radiographic diagnostics capable of improved imaging in two orthogonal directions. This goal was achieved (Fig. 104.64) and work is now proceeding to study the contributions of various initial modes to the enhanced spike penetration.

In the experiments, ten beams of the OMEGA laser irradiate a polyimide disk with UV light at an irradiance of $\sim 10^{15}$ W/cm^2 for 1 ns. This launches a 50-Mbar shock into the material, which later evolves to form a blast wave not unlike that produced during a supernova explosion. The blast wave crosses a structured interface to lower-density material, which is a surrogate for the structured interfaces that are present in a presupernova star. The subsequent, unstable evolution is monitored by radiographically detecting the structure of Bromine-doped
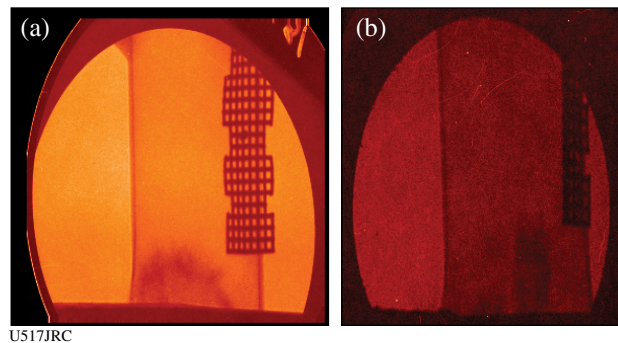

U517JRC

Figure 104.64
Data from the first experiments to obtain physics data using simultaneous, orthogonal, point-projection backlighting [viewing direction of image in (b) is orthogonal to that of (a)]. The data are obtained by using a brief (1 ns) x-ray source to project a signal onto an exposed piece of x-ray film. One can see on these images the structures that have evolved from an initial condition defined by $a_0 \sin(k_x x)\sin(k_y)$, where $a_0 = 2.5$ μm, $k_x = k_y = 2\pi/(71 \ \mu m)$. During the next year, the impact of a selected range of initial conditions will be studied.

material that was initially a strip within the high-density disk. The experiments can study some issues at a level of detail not possible in present-day simulations.

Astrophysical Jets and HED Laboratory Astrophysics
Principal Investigator: P. Hartigan (Rice University)

The series of experiments for the NLUF program on astrophysical jets and high-energy-density (HED) laboratory astrophysics was designed to explore what can be learned about astrophysical jets by simulating them in the laboratory while at the same time testing how well the advanced numerical codes *RAGE* and *PETRA* follow the evolution of shocked flows. In FY05, this program was granted one shot day on 25 May and another on 31 August. For the May shots, a series of baseline experiments were carried out to test the reproducibility of the jet creation. Results from these shots are shown in Fig. 104.65. The overall structure of the jet closely resembles that of the numerical simulations, and images taken at the same time from different shots are nearly identical in most cases. Hence, there is confidence that variations in the target construction are not dominating the experimental results. For the 31 August shots, a more advanced target design will be implemented in which a dense ball is embedded within the foam. This design shows many interesting shock waves in the numerical simulations and begins to address the astrophysical case of a jet deflecting from a dense molecular cloud or a jet entraining dense fragments within bow shocks. Such flows are of interest to astrophysicists as they are observed to occur in a variety of star formation
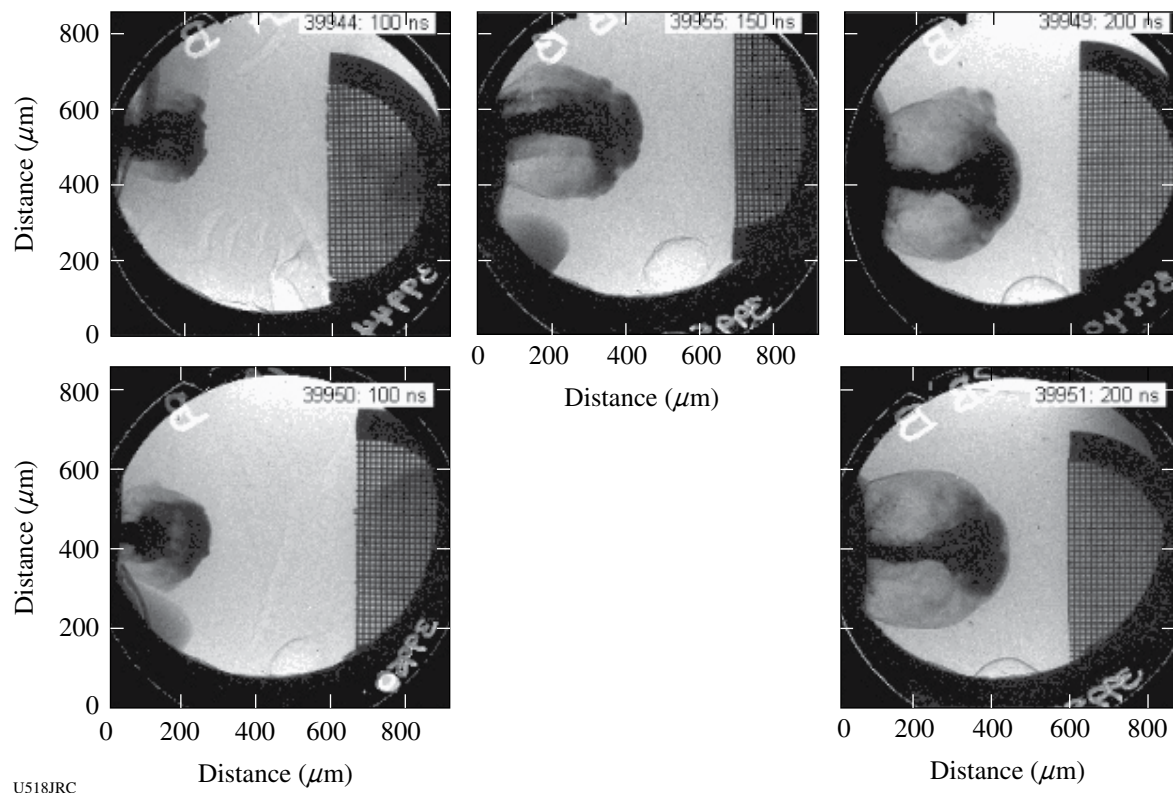
Figure 104.65
Time-framed x-ray backlit images showing the time evolution of jets on two OMEGA shots [39944 (top) and 39950 (bottom)].

settings and may help address issues such as the generation of turbulence in molecular clouds. The parameter space associated with dense clumps and shock waves is very rich, and it should be possible to explore a variety of phenomenon such as clump lifetimes, fragmentation, turbulence, and jet deflection for various sized clumps and impact parameters in future shots, provided these new targets perform as anticipated.

Creating the Core Conditions of Giant Planets in the Laboratory
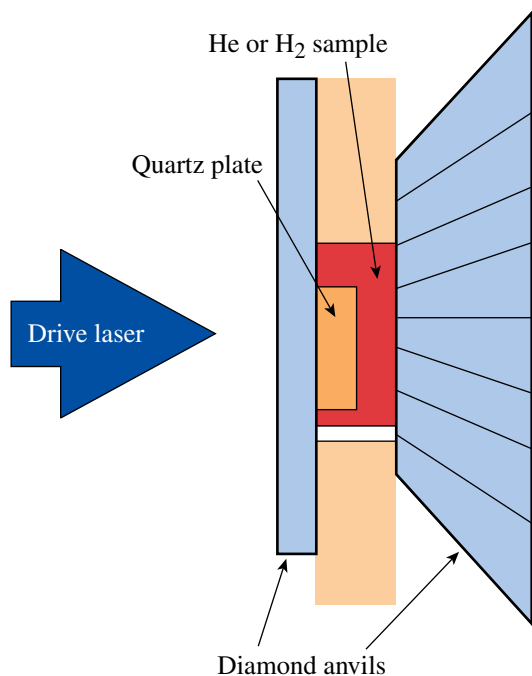Principal Investigator: R. Jeanloz (University of California, Berkeley)

During the past year, 13 OMEGA shots were conducted on diamond anvil cells filled with H_2, D_2, He, and He/H_2 mixtures. The primary focus of the work over the past year has been on dense He. Gas samples were precompressed (see Fig. 104.66) from 0.2 to 1.5 GPa and shocked to pressures as high as 200 GPa (2 Mbar). The experiments are designed to access the extreme densities of the interior regions of the giant

planets Jupiter and Saturn. The technique combines a diamond anvil cell target with a laser-driven shock. With this technique, the initial sample pressure is much higher than ambient (1 to 5 GPa), and the initial density may be from 1.5× to 4× higher than ambient (depending on the sample)—a large increase compared to nonpressurized preparation methods. Furthermore, in the important case of the He/H_2 mixtures that compose giant planets, precompression is the only way to produce a uniform single-phase target sample for high-pressure/density experiments. The higher initial density results in a significantly larger final density and correspondingly lower temperature in the shock-compressed state.

Using the active shock breakout (ASBO)/shock optical pyrometers (SOP) diagnostic, it was possible to determine pressure and density in the shocked sample as well as its optical reflectance. The temperature is simultaneously measured with the pyrometer capability of the diagnostic. Such equation-of-state measurements provide crucial constraints on models that describe planetary structure (current internal state) and internal

evolution, which is a key requirement for understanding the origins of planets. Electrical conductivity inferred from optical reflectance measurements are used as input data for models of planetary magnetic-field generation.

A quartz reference technique was employed for all of the samples tested to produce quantitative measurements of the Hugoniot parameters (P, V, and E), temperature (T), and shock-front reflectivity (R) that can be related to electrical conductivity (σ). The recent experiments provide measurements of the properties of dense He to the highest pressures yet achieved under shock compression. Detailed data are now available on the insulator-conductor transition in He at conditions near 1 g/cm^3 and ~2 to 5 eV; from these data it is estimated that the transition to metallic-like conducting states is near 360 GPa and 1 eV. This pressure is significantly lower than the esti-mated metallic transition along the cold compression curve (~1200 GPa). A significant data set on H$_2$ has also been col-lected at three different initial densities. These new data will provide an interesting comparison to the current extensive data set on cryogenic liquid deuterium. Finally, for the first time, two data points were produced on a 50% He/H$_2$ mixture. The preliminary Hugoniot results indicate that the compressibility of the mixture is consistent with an idealized mixing model
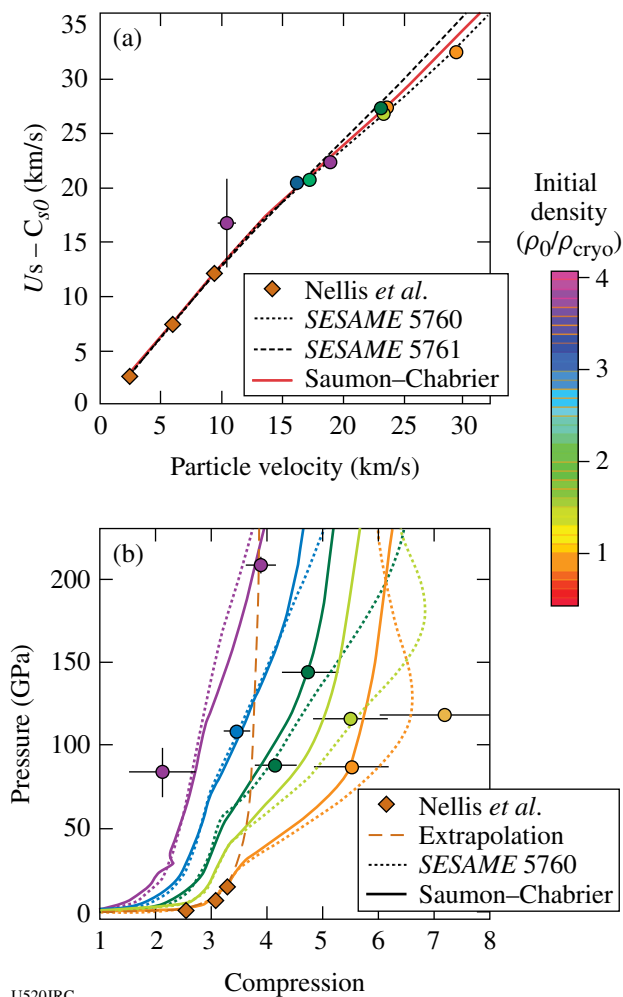
based on the equations of state of pure He and H$_2$; it is planned to increase this data set with the future OMEGA experiments that are currently being planned.

Figure 104.67(a) shows a compact representation of the He Hugoniot data plotted as a function of the particle speed. It turns out that all available theoretical models predict that the family of Hugoniot curves corresponding to an ensemble of precompressed states are parallel to each other and offset from

Figure 104.67
(a) He Hugoniot measurements plotted in a reduced form. Shock velocity minus the sound velocity of the initial state is plotted as a function of particle velocity. The shades of the points indicate initial density relative to the cryogenic liquid density (0.122 g/cm^3), as indicated by the scale. (b) Pressure as a function of compression for shock-compressed He at three different initial densities. Points show our data, the solid curves are predictions from the SCVH EOS, and the dotted curves are from the *SESAME* 5760 table. The dashed curve is an extrapolation of a linear fit to the low-pressure EOS data.

Figure 104.66
Schematic of the precompressed target arrangement.

the origin by the initial-state sound velocity. Different models predict different slopes for the Hugoniots, but all models are similar in that the Hugoniot for a range of precompressed states can be represented by a single average curve after the sound velocity offset is subtracted. Accordingly, the ordinate in Fig. 104.67(a) is given by the measured shock velocity minus the sound velocity of the initial state. As is evident in the figure, all of the data converge to a common reduced Hugoniot. Note that the slope of the high-pressure portion of the Hugoniot (particle velocity >10 km/s) is distinctly different from the slope of the low-pressure segment measured by Nellis *et al.*[2] The reduced slope observed for the high-pressure states indicates that the He Hugoniot undergoes a marked softening relative to its lower-pressure behavior. In this range, all the samples have become conducting, and thus the softening is probably associated with ionization.

Figure 104.67(b) shows the same data represented in terms of compression as a function of pressure. The near-vertical dashed line shows the behavior of the low-pressure Hugoniot if it is extrapolated to higher pressures—little can be said about compressions beyond about 3.5 because temperature dominates the pressure at this point (our precompression experiments avoid this problem). The solid curves show the behavior predicted by a commonly used astrophysical model calculated by Saumon, Chabrier, and van Horn (SCVH), and the solid curves show the same for the *SESAME* 5760 table. The softening at high pressures is predicted by both the SCVH and *SESAME* models. In addition to the Hugoniot EOS data, we extracted temperature and shock-front reflectance for cases where the latter was observable. These data are summarized in Fig. 104.68 for all of our He data set. The temperature data also show broad agreement with the SCVH EOS for He. The reflectivity data are strongly correlated with temperature, indicating that the driving mechanism for the conductivity is a thermal activation process.

The reflectivity data have been fit to a simple semiconductor model of the ionizing fluid. From the fit it is estimated that metallic-like conditions in dense He will be achieved near 2.7 g/cm^3 and 1-eV temperature, corresponding to ~360 GPa on the Jupiter isentrope. These data and the fit are also in good agreement with the data of Ternovoi *et al.*,[3] who measured the conductivity of dense He with a reverberating shock technique, and with the plasma–chemical model of Forster *et al.*[4] Figure 104.69(a) shows details of the fit to the semiconductor model; Fig. 104.69(b) shows the estimated metallization boundary on the pressure-temperature (P-T) phase plane.
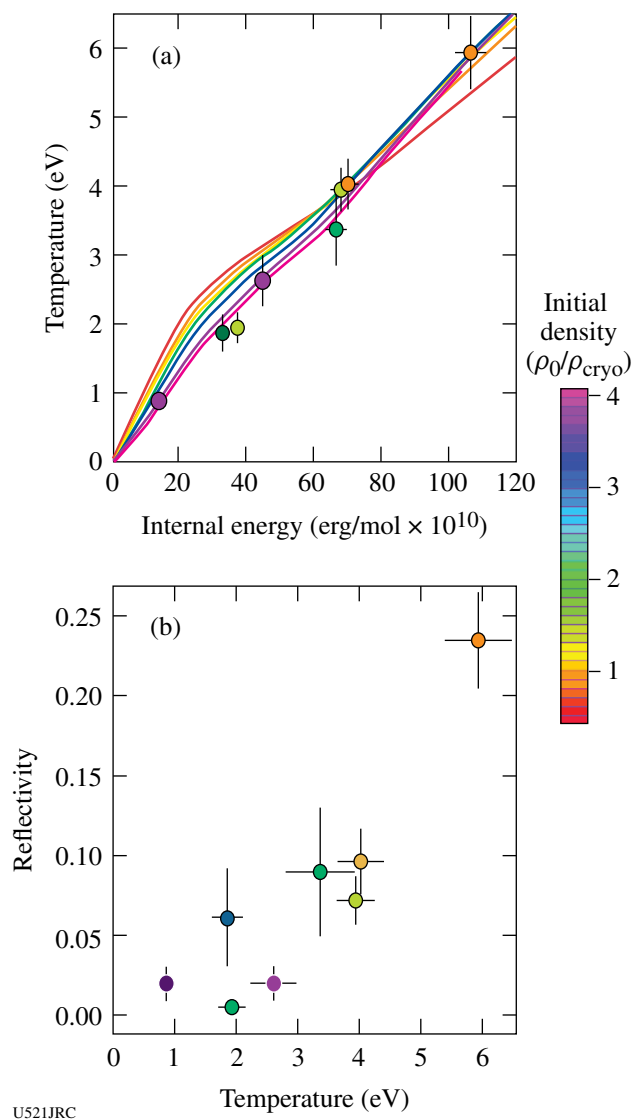

Figure 104.68
(a) Temperature as a function of internal energy for He (points) in comparison with the SCVH model (solid curves); the tone scheme is the same as described in Fig. 104.67. (b) Reflectivity as a function of temperature for shock-compressed He.

In addition to the He results, high-pressure data on H_2 continued to be collected, and Hugoniot data have been obtained, centered at three different initial densities (not shown here). Analysis of these data is ongoing, as the completion of an accurate model for the release response of the quartz standard is in progress. This will be the first high-pressure data set available to compare the high-pressure response of H_2 with the current extensive set of data for shock-compressed D_2.
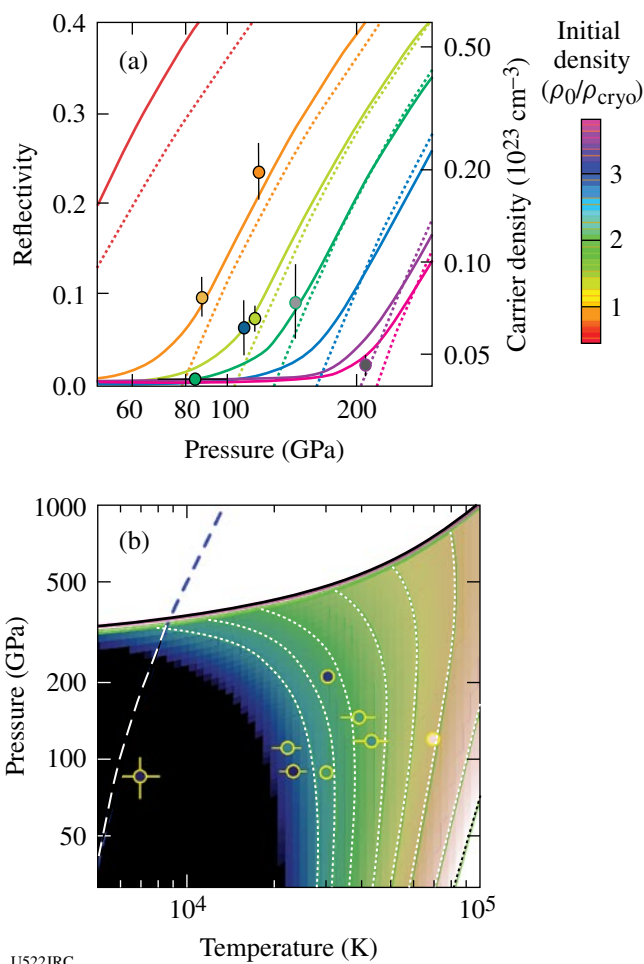
Figure 104.69

(a) Reflectivity of He as a function of shock pressure in comparison with a semiconductor model fit (solid curves). Dashed curves show the corresponding carrier density (right scale). (b) Points show the locations on the P-T plane of the data points in (a). The dotted curves and the tonal scale show contours of constant ionization from the model, the thick solid curve is the 2.7 g/cm^3 isochore (indicating the metallization boundary), and the dashed curve is the Jupiter isentrope.

Finally, the first two experiments on He/H$_2$ mixtures have been completed. The Hugoniot results, shown in Fig. 104.70, indicate that the compression curve of the mixture is well modeled by an equation of state constructed by linear mixing of the SCVH He and Ross H$_2$ models. This is work in progress; considerably more analysis must be performed and more data collected before strong conclusions can be made.

Currently, a wide range of states in He and H$_2$ have been explored, and the first two experiments on He/H$_2$ mixtures

have been performed. For the coming year, this investigation will focus on He/H$_2$ mixtures. Because they are immiscible fluids, at ambient pressure and low temperature, these mixtures have never been studied at high pressures. The studies will begin to address the issues of He/H$_2$ miscibility, the transition to conducting states in the mixture, and the effect of the mixture on the equation of state. The conductivity (inferred from reflectance) in He/H$_2$ mixtures allows the determination of ionization properties. These data will provide insight on the electrical conductivity and the miscibility of He/H$_2$ mixtures in the giant planets.
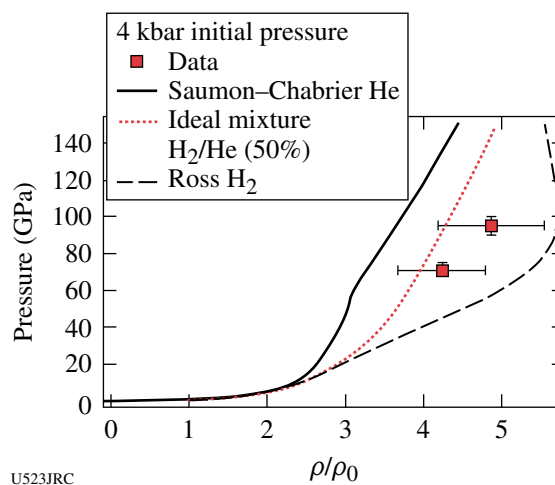

Figure 104.70

(a) Initial Hugoniot data on a 50% mixture of He/H$_2$, shown in comparison with a theoretical Hugoniot calculated based on ideal mixing of the SCVH-He model and the Ross H$_2$ model.

Three-Dimensional Study of the Spatial Structure of Direct-Drive Implosion Cores at OMEGA
Principal Investigator: R. Mancini (University of Nevada, Reno)

The goal of this project is to determine the three-dimensional spatial structure of temperature and density distributions in high-energy-density core plasmas arising from OMEGA direct-drive implosions. Targets are plastic shells with a gas fill made out of deuterium and a tracer amount of argon for spectroscopic diagnostics. The data for the analysis consists of space-integrated, time-resolved x-ray argon line spectra recorded with streaked crystal spectrometers and gated x-ray narrow-band images based on argon line spectral features obtained along three quasi-orthogonal directions.

Data modeling and analysis is performed using a spectral model that considers collisional-radiative level population kinetics, detailed Stark-broadened line shapes for both resonance- and satellite-line transitions, and radiation transport. Two analysis methods have been developed to extract temperature and density gradients from the data. On the one hand, using emissivity maps obtained from image data inversion temperatures are determined from narrow-band emissivity ratios and then densities are computed by solving a set of emissivity equations. On the other hand, a search and reconstruction algorithm driven by a Pareto genetic algorithm searches parameter space for the temperature and density gradients that yield the best simultaneous fits to the space-integrated line spectrum and a set of narrow-band emissivity maps and image intensity distributions, i.e., multi-objective data analysis.

Three multimonochromatic x-ray imagers (MMI) were designed, built, and fielded in OMEGA direct-drive implosion experiments during FY05. These (identical) instruments recorded gated narrow-band x-ray images of the core along three quasi-orthogonal directions at the collapse of the implosion based on the Ly_α, He_β, and Ly_β (and associated Li- and He-like satellites) line transitions of argon. In addition, a pre-existing x-ray imager at OMEGA was modified for better performance and fielded in the same experiments to obtain another Ly_β image along a direction diametrically opposite to one of the MMI's line of eight. This extra image permits an experimental check on the opacity of the Ly_β line emission in the core. Work is in progress in the analysis of the data.

Implosion Dynamics and Symmetry from Proton Imaging, Spectroscopy, and Temporal Measurements
Principal Investigator: R. D. Petrasso (Massachusetts Institute of Technology)

NLUF Proton Radiography Experiments

Initial experiments were conducted on OMEGA as part of this NLUF program to explore the use of proton radiography to study transient electric and magnetic fields generated by the interaction of OMEGA laser beams with plastic foils. In each experiment, a plastic foil was illuminated by a single OMEGA laser beam, and a projection radiograph was made of the foil using a source of nearly monoenergetic 14.7-MeV protons and a CR-39 area detector for image recording. The

protons passed through a wire mesh (see Fig. 104.71) before impinging on the foil, and the distortion in the mesh pattern at the detector shows how the proton trajectories were deflected through interaction with the fields generated by laser–plasma interaction at the foil.

The proton source for these experiments was formed by imploding a D^3He-filled, glass-shell capsule with 20 OMEGA laser beams in a 10-kJ, 1-ns pulse. The capsule diameter of the proton source target was unusually small, at about 440 μm, in order to provide a smaller-than-usual burn radius for optimal spatial resolution in the radiograph; the full width at half maximum (FWHM) of the proton source was about 50 μm, measured with proton emission imaging. The mesh was mounted on the foil assembly about 1 cm away, and the center-to-center spacing of the mesh wires was either 150 μm or 200 μm. The CR-39 detector was about 36 cm away. The burn duration of the D^3He implosion was short (~100 ps) relative to the 1-ns duration of the foil illumination; adjusting the timing of the implosion relative to the foil illumination allows images to be recorded at different times. Sample images are shown in Fig. 104.72. Magnetic fields of the order of ~0.5 MG in the vicinity of the laser-irradiated foil are estimated on the basis of the proton deflection observed on these images (see Fig. 104.73).
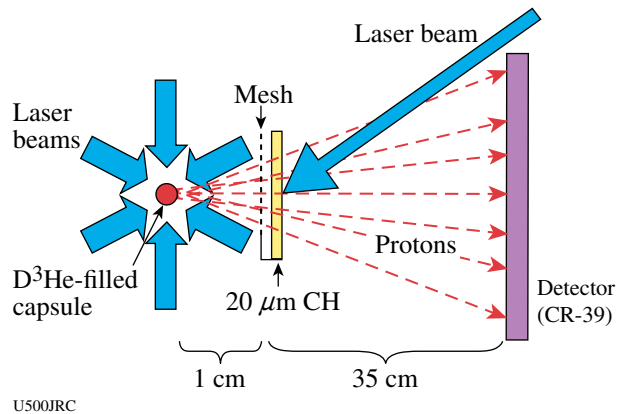

U500JRC

Figure 104.71
Physical arrangement of the proton backlighter (imploded D^3He-filled capsule), mesh, CH foil, CR-39 imaging detector, and OMEGA laser beams, as used for radiography.
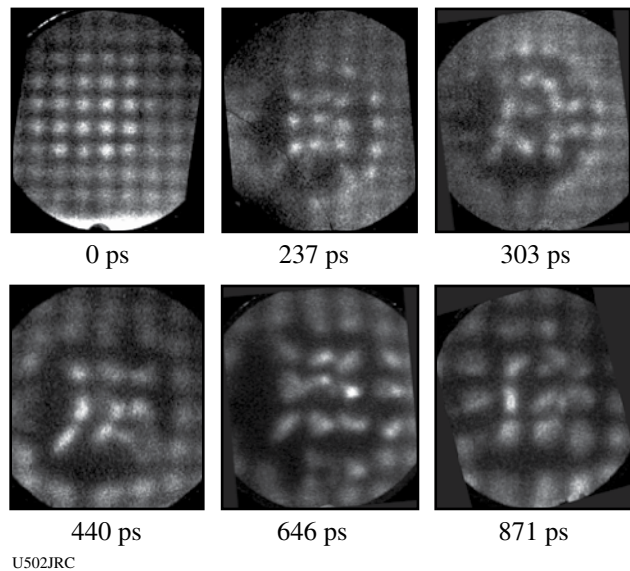
Figure 104.72
Images recorded on the CR-39 detectors during different OMEGA shots. Each image is labeled by the difference between the time at which the protons passed the foil and the time when the foil was struck by a laser beam. The first three images were made using a mesh with 150-μm (center-to-center) spacing, while the last three were made with a 200-μm mesh.
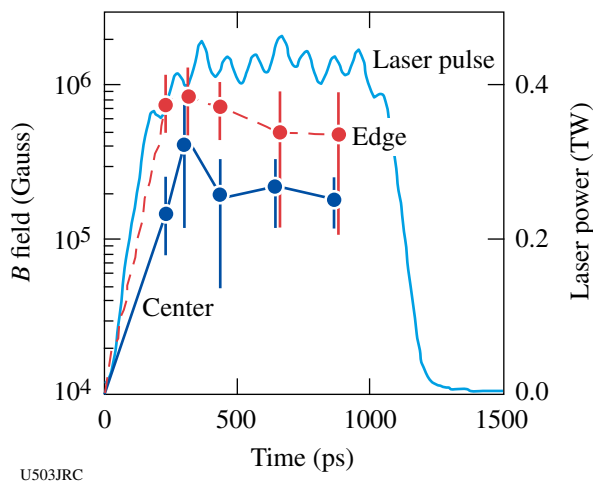

Figure 104.73
Time evolution of magnetic-field amplitude at two locations on the laser-irradiated foil (center and edge of the laser beam)—referenced to the plasma-generating laser pulse (thick solid line).

LLNL Experiments on OMEGA in FY05

During FY05, LLNL was scheduled for 372 shots on OMEGA. These were distributed into 191 planned shots for the Inertial Confinement Fusion (ICF) program, and 181 planned shots for the High-Energy-Density Sciences (HEDS) program. The actual OMEGA performance averaged 7.5% more shots than scheduled (400 shots). A brief summary of the various campaigns follows, starting with HEDS experiments.

Hot Hohlraum Experiments: Hot hohlraum experiments were carried out; their objectives were to explore the laser–plasma interaction limits of very small half-hohlraums ("halfraums") and to maximize the effective radiation temperature. Figure 104.74 shows x-ray images recorded at various times and photon energies, which show the hohlraum filling to overcritical densities.

Hohlraum Development: In hohlraum development experiments, high-Z foam (approximately 5% of solid density) was substituted for solid gold for the hohlraum wall and measured a predicted increase in x-ray conversion efficiency.

Double-Shell Capsules: Pusher single-shell experiments used a glass capsule (coated with a plastic ablator) to explore physics issues associated with double-shell capsules.

Isentropic Compression Experiments (ICE): Isentropic compression experiments used a carefully shaped laser pulse to create a smoothly increasing, shockless compression of various target materials for equation of state measurements. These included diffraction experiments where x-ray diffraction from crystalline materials was used to diagnose change of state. Low-temperature Rayleigh–Taylor experiments also used the isentropic drive to investigate the hydrodynamic stability of solid materials under strong acceleration.

X-Ray Backlighting Development: Backlighter capability experiments were conducted with the aim of improving the x-ray backlighting capabilities. These experiments included backlit pinholes for point-projection measurements as well as various mid-Z (e.g., Ti) doped foams for increased x-ray conversion efficiency into multi-keV photons.

Radiation Flow: Radiation flow experiments continued from the previous year. These experiments used foam-filled hohlraums to measure x-ray propagation through various low-density materials.
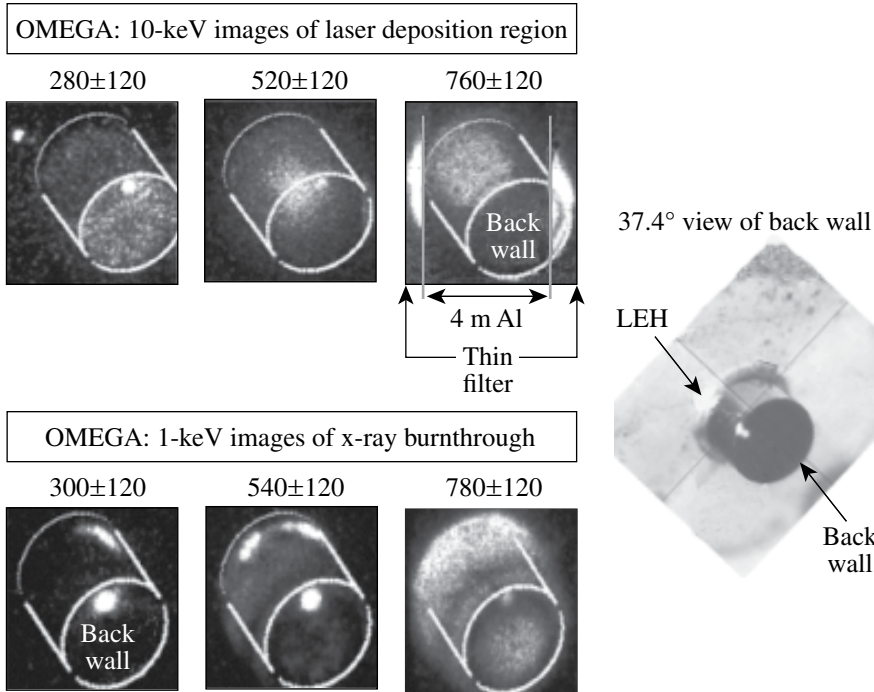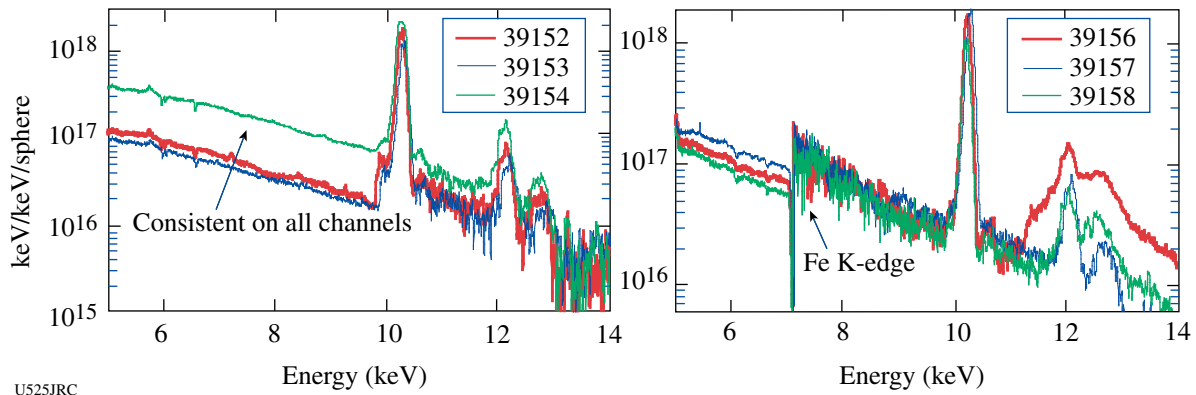
OMEGA: 10-keV images of laser deposition region

280±120   520±120   760±120

Back wall

4 m Al

Thin filter

OMEGA: 1-keV images of x-ray burnthrough

300±120   540±120   780±120

Back wall

U524JRC

37.4° view of back wall

LEH

Back wall

Figure 104.74
X-ray images of "halfraum" plasma fillings (view is 37.4° to the back wall). The time is given in picoseconds. The 10-keV images show that the laser deposition region moves from the back wall toward the LEH. The 1-keV images show that burnthrough occurs first near the LEH.

NWET: NWET (effects test) experiments concentrated on fielding multiple diagnostics to measure electromagnetic pulse and x rays from laser-driven hohlraums filled with low-density, mid-Z foams. These experiments were a collaboration between LLNL, LLE, and NRL and required the extensive installation of specialized diagnostics. Figure 104.75 shows the x-ray spectra recorded from 5-mg/cc aerogel (silicon dioxide) foam, doped with 20 atom-% Ge. Such targets produced an overall conversion efficiency of ~0.3% into x rays in the 9.4 to 13.8 keV range.

Opacity: An extensive opacity campaign was conducted on OMEGA. Early experiments were dedicated to developing appropriate x-ray backlighting sources, leading to future measurements of the opacity of warm materials.

Planar Double Shell: Planar double-shell experiments using a geometry that allowed diagnostic access were carried out to investigate the effects of x-ray preheat on the inner shell of a double-shell capsule.

U525JRC

Figure 104.75
Sample x-ray spectra obtained using the HENWAY spectrometer from targets containing SiO_2 foam (aerogel) at a density of ~4.8 mg/cc doped with 20 atom-% Ge. These data indicate x-ray yields ranging from 50 to 100 J for Ge K-shell radiation. On shots 39152 to 39154, the continuum is from 12-μm Al and 1-mil Be strips and T_e ~ 2.5 to 2.8 keV. On shots 39156 to 39158, the continuum features are due to a 12.6-μm Fe foil, T_e ~ 2.0 to 2.4 keV.
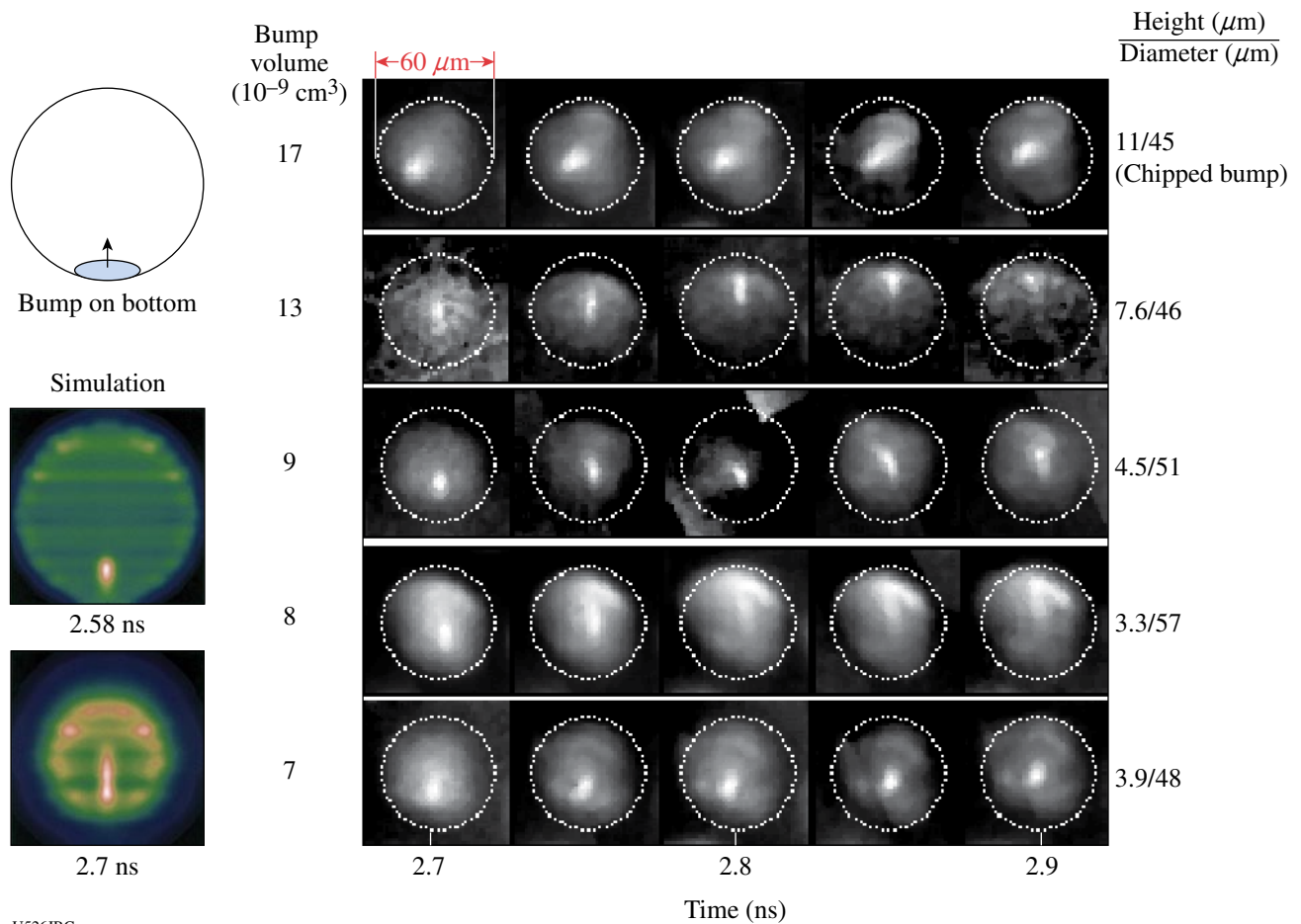
DPP: A series of experiments dubbed DPP investigated jets of material driven into foams with varying cell sizes. X-ray backlighting was used to measure the propagation of the jets into the foams.

Low- and Mid-Z Liners: The first ICF experiments of FY05 were designed to investigate laser–plasma issues and x-ray drive measurements of hohlraums with low- and mid-Z liners and foam fills. These liners and foams are designed to inhibit inward motion of the hohlraum walls and are an alternative to gas-filled designs.

Fill Tubes: A campaign was initiated to investigate the effects of fill tubes on capsules. These indirectly driven capsules used a single perturbation on the surface of the capsule to simulate, in a calculable way, the effect of an actual fill tube on the hydrodynamic stability of the shell. Figure 104.76 shows high-magnification x-ray images of such targets. The

perturbation grows and produces a jet of mid-Z material (originally implanted in the inner wall of the capsule). This material becomes visible in x-ray wavelengths as it is heated by the hot core.

Gas Hydro: "Gas-hydro" experiments were carried out using large, plastic, gas-filled hohlraums with a foam ball at the center. The objective of this campaign was to reduce the x-ray drive so that the direct, hydrodynamic effects of the laser-heated fill gas on a capsule could be observed and compared with simulations. Figure 104.77 shows the results of the first of such attempts. The shock front in the foam surrogate target, observed with x-ray backlighting, shows the effects of the laser-heated gas pressure for low initial fill pressures. Contrary to simulations, however, no effect was observed at higher initial fill pressures. A new experiment, designed to have reduced sensitivity to target alignment, will explore these issues.

Figure 104.76
Simulations (left) and x-ray framing camera images of capsules with imposed bumps that are used to simulate a fill tube.
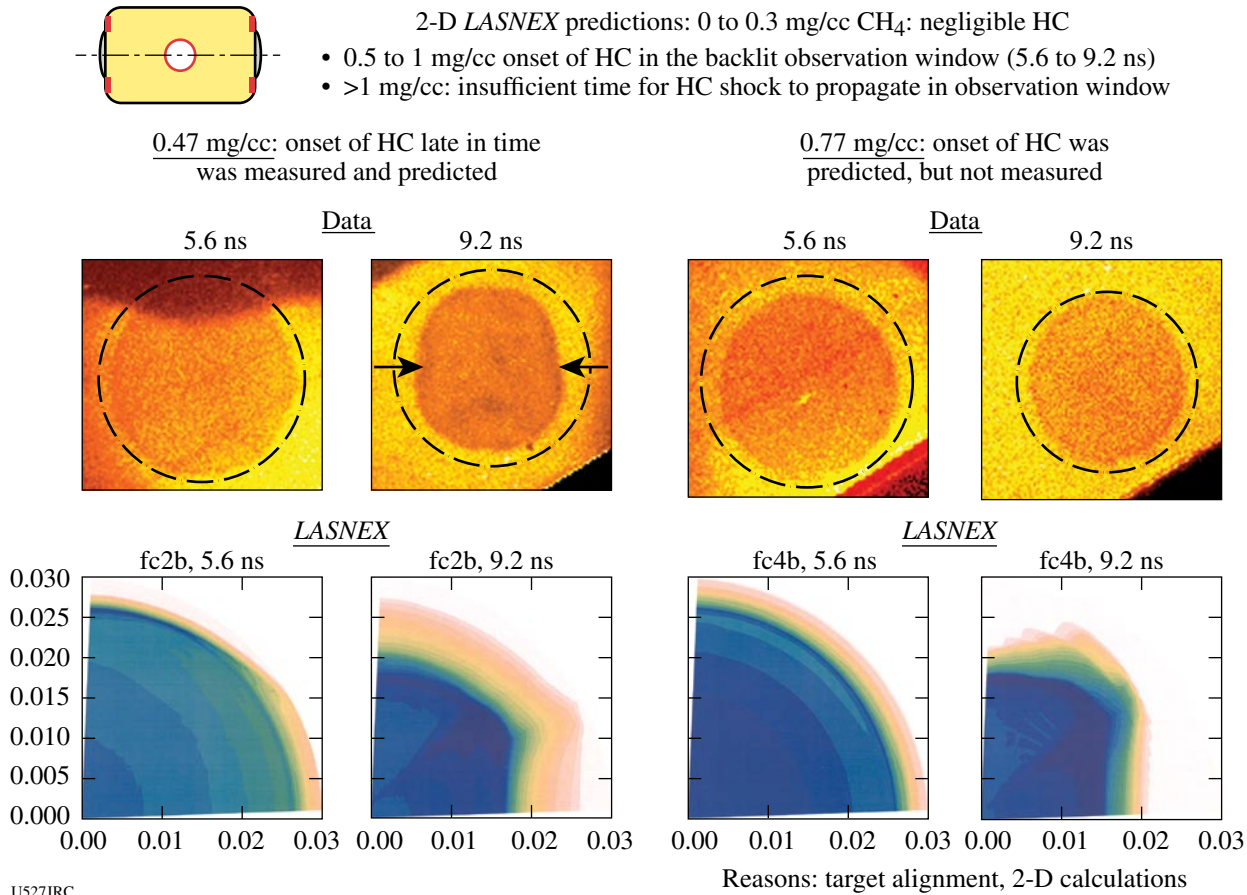
2-D *LASNEX* predictions: 0 to 0.3 mg/cc CH$_4$: negligible HC
- 0.5 to 1 mg/cc onset of HC in the backlit observation window (5.6 to 9.2 ns)
- >1 mg/cc: insufficient time for HC shock to propagate in observation window

0.47 mg/cc: onset of HC late in time was measured and predicted

0.77 mg/cc: onset of HC was predicted, but not measured

Data

5.6 ns   9.2 ns

Data

5.6 ns   9.2 ns

LASNEX

fc2b, 5.6 ns   fc2b, 9.2 ns

LASNEX

fc4b, 5.6 ns   fc4b, 9.2 ns

Reasons: target alignment, 2-D calculations

U527JRC

Figure 104.77
X-ray images from "gas-hydro" experiments. Top: X-ray backlit images of foam targets in 0.47 mg/cc and 0.77 mg/cc CH$_4$-filled hohlraums. Bottom: *LASNEX* simulations showing effects of gas hydrodynamics coupling to the implosion. The onset of hydrodynamic coupling was measured and predicted at low fill density but not observed at high density.

RTI in Be-Doped CH: Experiments were conducted to develop a Rayleigh–Taylor instability platform for accurately measuring the Rayleigh–Taylor growth rate of Be and Be doped with Cu ablators in direct comparison with more traditional CH ablators.

HEP-4: The HEP-4 series of implosions are integrated experiments that use standardized hohlraums and laser pulse shapes while varying the surface finish of the capsules by deliberately roughening them. The resulting neutron yields are compared to simulations with capsule-fuel mix models; the initial measured capsule perturbation spectrum is included in the simulation for each capsule to enable direct comparison with the experimental results. These experiments have been carried out on OMEGA for some time and were completed this year. Results are shown in Fig. 104.78.

Cocktail Experiments: "Cocktail" experiments were measurements of the effective x-ray drive power in hohlraums made of a mixture of high-*Z* materials (typically Au, Dy, U), in contrast to a single material. In FY05, considerable research and development from target fabrication at LLNL and GA was applied to reduce the impurity level of oxides in these targets, leading to measured unambiguous expected increases in x-ray flux (Fig. 104.79).
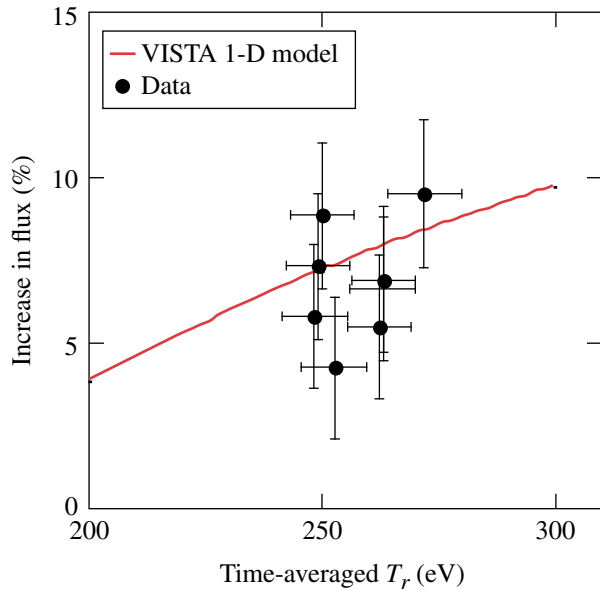
2ω LPI Experiments: A week of experiments was done with beam 25 converted to 2*ω* (530 nm). Measurements of laser–plasma interaction physics with "green" light were done in both hohlraum and open (using gas-bag targets) geometries. Figure 104.80 shows measurements from a 2*ω* beam that was propagated axially along a laser-heated hohlraum. Measurements of the 2*ω* beam transmission and stimulated backscatter

are shown. In addition, experiments were done with half-hohlraums to measure the overall x-ray conversion efficiency of 2ω light in direct, simultaneous comparison to the efficiency when using the 3ω light typical of OMEGA.
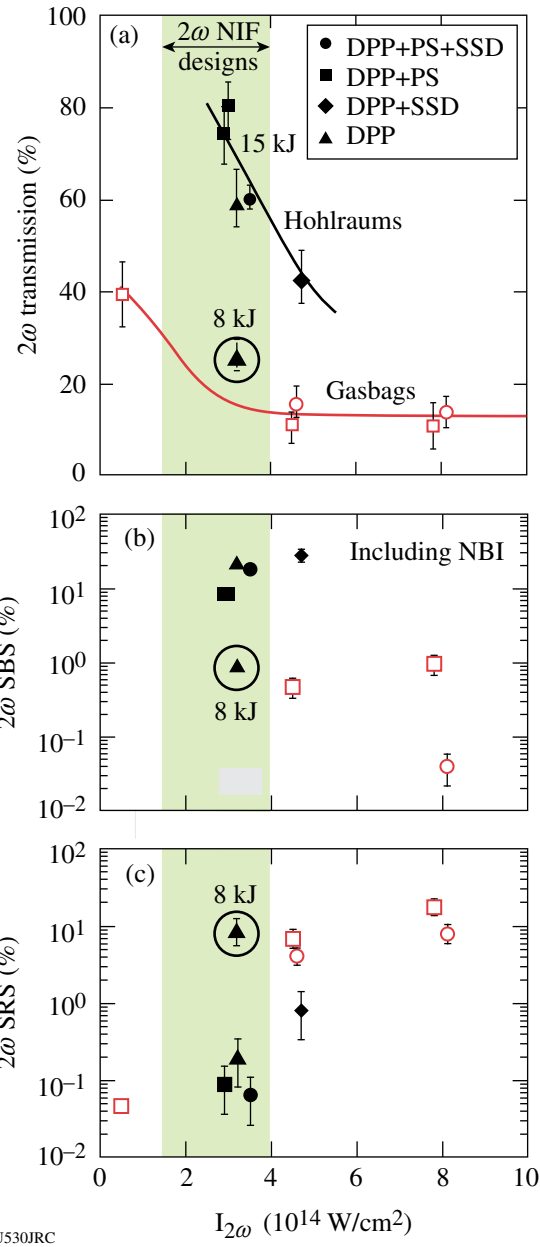

U528JRC

Figure 104.78

Neutron yield as a function of capsule roughness for HEP-4 experiments. Large filled data points were obtained in April 2005. Small open dots are smooth capsule data and square data were obtained in the prior campaigns.

U529JRC

Figure 104.79

A plot of the measured (black dots) and VISTA 1-D model predicted an increase in x-ray flux of a cocktail hohlraum with a composition of $Au_{0.2}U_{0.6}Dy_{0.2}$ versus conventional Au hohlraums as a function of time-averaged radiation temperature (T_r).

U530JRC

Figure 104.80

(a) Plots of 2ω beam transmission through a hohlraum (solid data points) and through gas bags (open points). Similar comparison for SBS (b) and SRS (c).

Plan "B": After encouraging laser–plasma interaction physics were obtained from SiO_2 foam-filled hohlraums, a series of foam-filled hohlraums with implosion capsules inside them were shot ("Plan B"). These yielded results similar to traditional vacuum hohlraums, indicating little or no deleterious effects on the x-ray drive for ICF-relevant foam fills.

X-Ray Thomson Scattering: X-ray scattering experiments were carried out, showing expected spectral features after scattering a strong line source from the hot plasma. The data were used to infer an electron temperature in the plasma.

4ω Thomson Scattering: A week of experiments was done with beam 25 converted to 4ω (260 nm). The principal focus was using the 4ω light for Thomson scattering measurements. Numerous improvements were made to the diagnostics from previous experiments, and the resulting data was of high quality, enabling the measurement of the electron temperature immediately external to a hohlraum laser entrance hole and from within a hohlraum. Figure 104.81 shows the Thomson-scattering-derived electron temperature from within a gas-filled hohlraum for three different laser energies. Careful characterization of these hohlraums is preliminary to their future use for LPI studies.

FY05 LANL OMEGA Experimental Programs

Los Alamos National Laboratory (LANL) successfully fielded a range of experiments on OMEGA during FY05 to study the physics relevant to inertial confinement fusion (ICF) and high-energy-density (HED) science in support of the National ignition effort. Many of these experiments were focused on developing underlying physics, diagnostics, and platforms for future experiments on the National Ignition Facility (NIF). LANL conducted a total of 138 target shots on OMEGA. Collaborations with LLNL, LLE, and AWE remain an important component of LANL's program on OMEGA. With the consolidation of ignition research in the United States into the National Ignition Campaign (NIC), healthy partnerships are required to achieve success in our National scientific objectives.
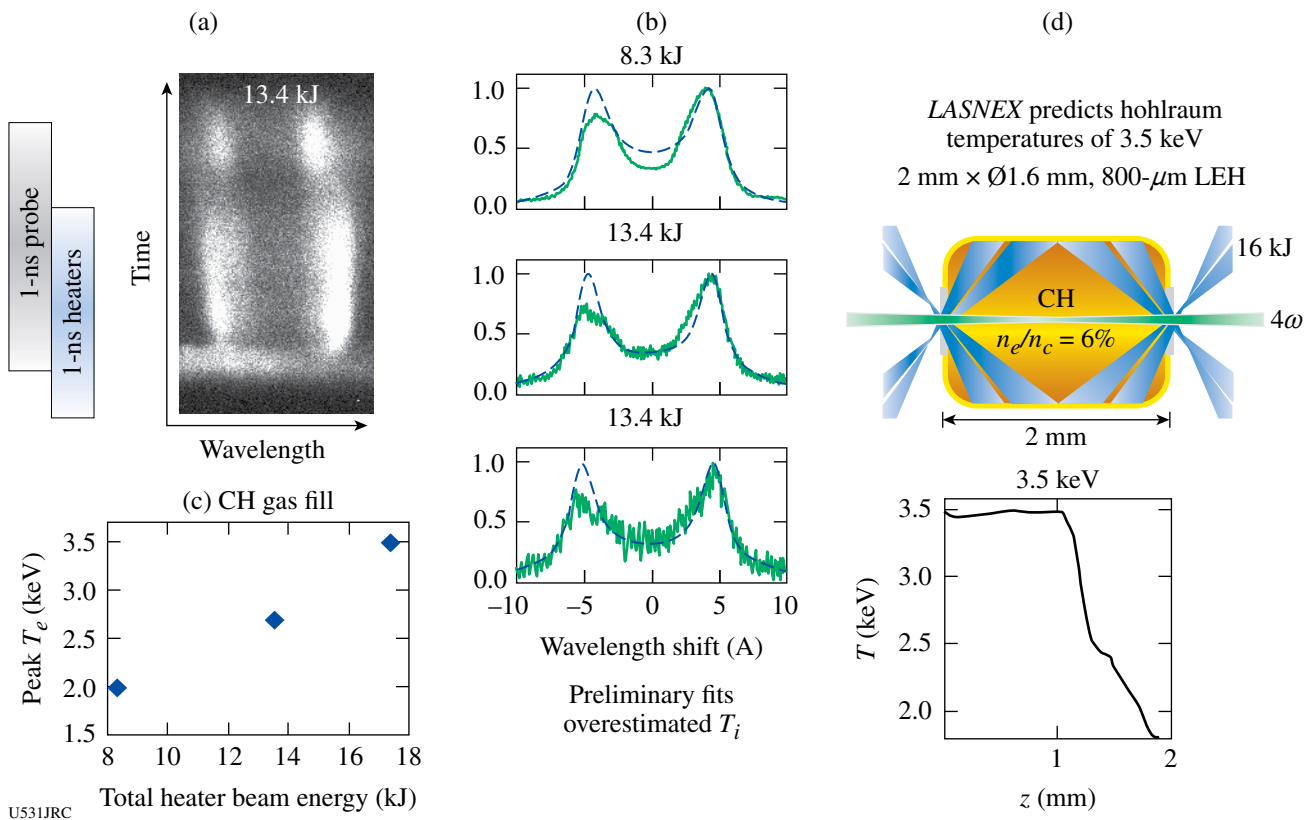

Figure 104.81
Data from 4ω Thomson scattering experiments: (a) streak camera record of spectrally resolved Thomson scattering spectrum, (b) scattering light spectra at various heater beam energies, (c) inferred electron temperature from these spectra, and (d) *LASNEX* predictions.

Beryllium Ablator Microstructure Stability (BAMS): The end goal of this project remains the delivery of a specification for the microstructure of ignition-capsule ablators to the National ICF program with the current focus on beryllium–copper ablators with 0.9% Cu by atom.

Two days of experiments using gas-filled hohlraums demonstrated the fabrication of small-amplitude Be sinusoids and measured growth of the sine wave perturbations in Be in a radiation-drive environment for the first time. The composite laser pulse consists of a combination of two separate OMEGA pulse shapes with a duration approaching 6 ns. Through VISAR measurements, a ~1-Mbar first shock in the Be (Cu) samples was observed. The methane gas fill held the Au walls of the hohlraum back for >10 ns to enable late-time, face-on x-ray radiography, thus demonstrating the growth of the sinusoid and evolution toward a spike-and-bubble behavior. Figure 104.82 shows a face-on, 1.7-keV radiograph of a sinusoid taken at 9.3 ns after the drive began. A lineout showing spike-and-bubble formation is illustrated in Fig. 104.83. The loss of laser energy to laser–plasma instabilities is modest (<10%), concentrated late in time, and clamps the radiation temperature near 145 eV.

In x-ray sidelighting experiments, differences between powder-pressed Be samples and sputtered samples as they are ejected from the hohlraum were observed. This difference may be related to excessive voids in the sputtered samples. The LANL theoretical group is modeling the shock breakout and
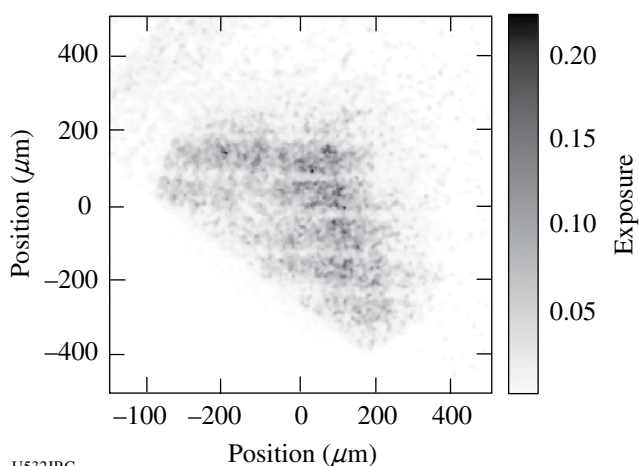

Figure 104.82
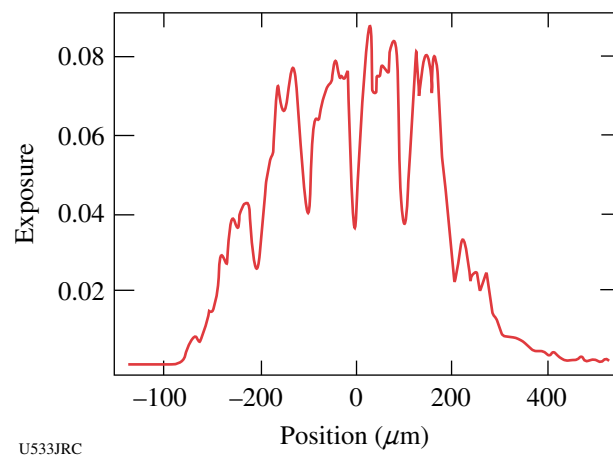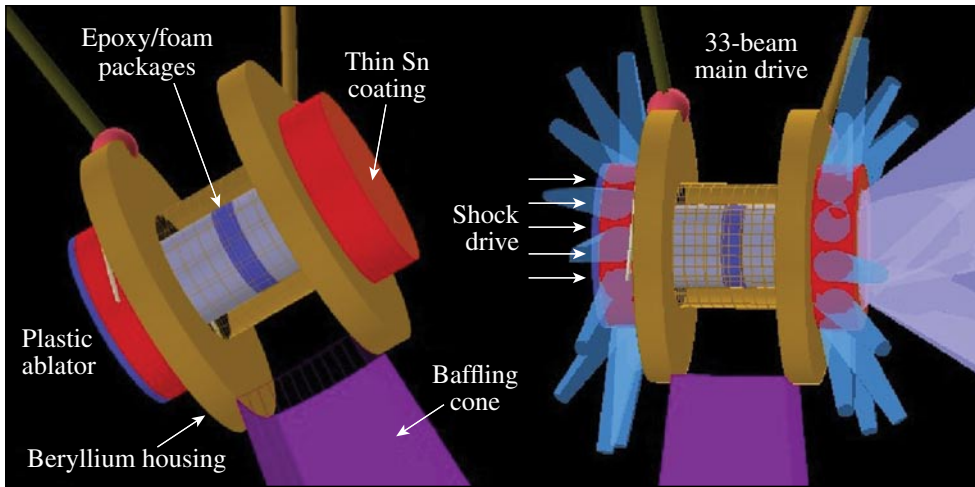A face-on radiograph of a BeCu sinusoid (shot 39660) at 9.3 ns after the start of hohlraum drive.

Figure 104.83
A lineout from the 9.3-ns data showing the growth of the sinusoidal perturbations and bubble–spike formation.

preheat of the BeCu samples to reproduce the as-measured radiation drive and to duplicate the "rollover" in growth rates of the instability growth with large-amplitude (2.5-μm) sinusoids.

Off-Hugoniot Stability: The off-Hugoniot (OH) campaign studies material dynamics under heated and shocked conditions. In ignition capsules, defects arising from the manufacturing process undergo significant evolution because of heating from Au M-band radiation prior to the passage of the main shock. It has not been demonstrated that the hydrocodes being used to model these experiments accurately capture the physics of this interaction. The OH platform provides the means to study the complex interactions between shocks and heated material.
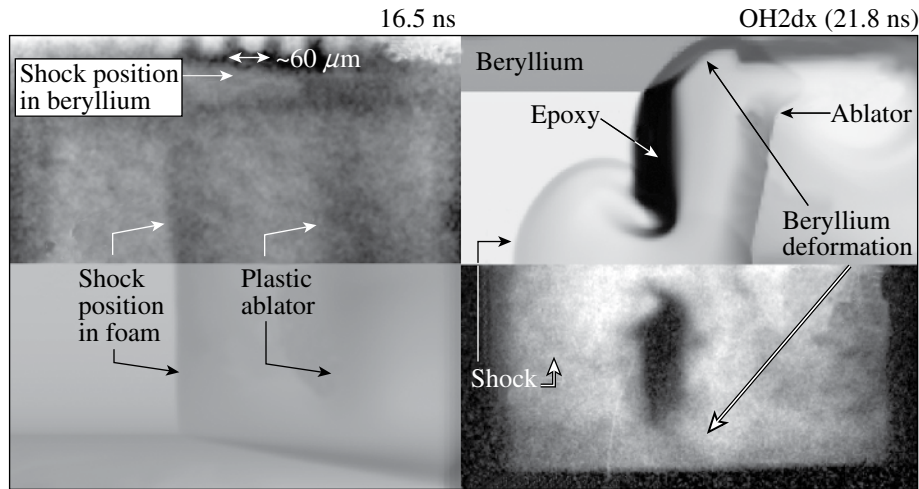
The OH platform utilizes a Be housing that is coated with a thin layer of tin. Inside the housing are layers of foam and epoxy. Thirty-three beams strike the tin, produce L-shell radiation that permeates throughout the package, heating the epoxy and foam (Fig. 104.84). A short time later, seven beams launch a strong shock into the foam. As the heated epoxy expands in the foam, the shock interaction with this system is imaged radiographically.

This year, the last phase of test bed development was completed in which shock planarity and speed were characterized and the interaction with an unheated defect was observed (Fig. 104.85). The next phase of campaign will advance to the fully integrated experiments of shock interaction with preheated material interfaces.

Figure 104.84
The target configuration for the off-Hugoniot experiment. A beryllium housing stuffed with layers of epoxy and foam are heated by exciting tin L-shell radiation. The evolution of the epoxy expanding into the foam is imaged via radiography.

Figure 104.85
(a) Comparisons between measurement and simulation (*RAGE*) of the shock position and planarity and (b) the unheated defect having experienced a strong shock.

Double-Shell Implosions: Double-shell implosions may provide a noncryogenic path ICF. Because of their complex implosion dynamics, however, double-shell capsules are much more sensitive to symmetry than their single-shell counterparts. Moreover, engineering defects, such as gaps formed during manufacturing, can play a large role in affecting their fusion yield.
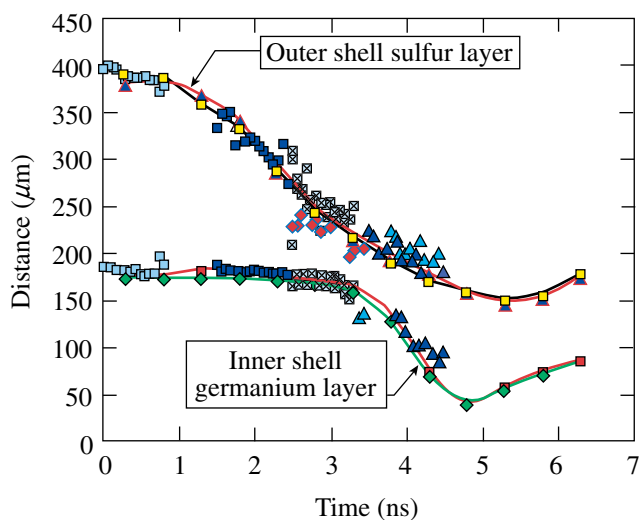
To better understand these issues, two experimental campaigns were conducted on OMEGA. The first characterized the zero-order implosion dynamics of a double-shell capsule implosion. The second measured how a gap purposefully machined in the outer shell evolved throughout the implosion. Selected results are presented.

Figure 104.86 shows the measurements of the inner and outer shell positions as compared with the simulated radiographs from *LASNEX*. Figure 104.87 displays a pre-shot radiograph and obtained shot data from a double-shell implosion with a deliberate engineering defect applied to the interior side of the outer surface. This data is used to quantify the defect's impact on the implosion symmetry.

Inhomogeneous Radiation Flow: Radiation transport calculations become greatly complicated in regions where two or more materials are inhomogeneously mixed. Laboratory experiments were performed to test the modeling of radiation transport through inhomogeneous plasmas.

A laser-driven hohlraum creates a radiation front, which propagates through a foam/gold particle mixture (Fig. 104.88). The position of the radiation front is measured as a function of time with a soft x-ray imager (Fig. 104.89). Three different foam–gold mixtures were examined experimentally (Fig. 104.90). One mixture was purely foam, another mixture was loaded with 2-μm-diam gold particles, and the last mix-

ture was loaded with 0.5-μm-diam gold particles. Each of the doped foams contained the same amount of gold volumetrically. Preliminary results from these experiments show the radiation front propagation slows in the presence of smaller gold particles. The next set of planned experiments have the objective of making a single temperature measurement of the radiation front.

Beryllium Fill-Tube Defect Studies: Current ignition target designs for the NIF use a copper-doped beryllium (BeCu) ablator. Since DT cannot diffuse through the Be ablator, another filling method is required. The leading option is to use a fill tube, however, the tube provides a perturbation on the capsule that may affect the ignition capsule implosion. Initial experiments were performed that developed a planar platform to investigate the effect of a fill tube on ICF capsule performance.

The experimental configuration (Fig. 104.91) consists of a driven hohlraum, which heats and shocks the attached Be (0.9% Cu). Beryllium material then jets through the hole and into the surrounding vacuum. Two backlighters are used to image different aspects of the experiment. An iron backlighter resolves the shock position in the Be disk. A Teflon (C2F4) backlighter captures the jet with its C and F He-α lines (310 eV and 740 eV, respectively) using the soft x-ray imager. We also obtained images with the Teflon continuum. A definite jet was observed (Fig. 104.92) with a 30-μm-diam hole. The jet has a length and width of the order of 100 μm. This series of experiments validate the planar platform, which will be used by NIC in future experiments.
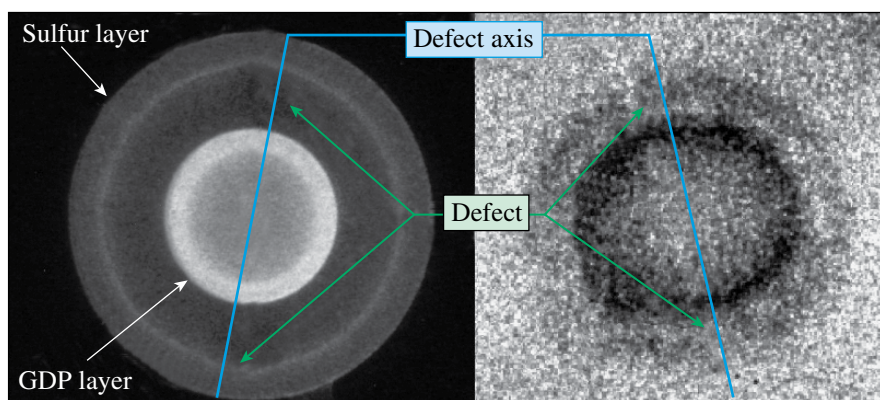

U536JRC

Figure 104.86
Measurements (symbols) of the outer and inner shell marker layers, showing collision near 3.6 ns. The solid lines are the *LASNEX* predictions as extracted from the simulated radiographs.

U537JRC

Figure 104.87
(a) A preshot radiograph of a defect capsule.
(b) An image of the implosion near 3.8 ns showing the interaction between the defect and inner shell.

U538JRC

2. Radiation front propagates
   through doped foam

3. Radiation
   front
   tracked via
   soft x-ray
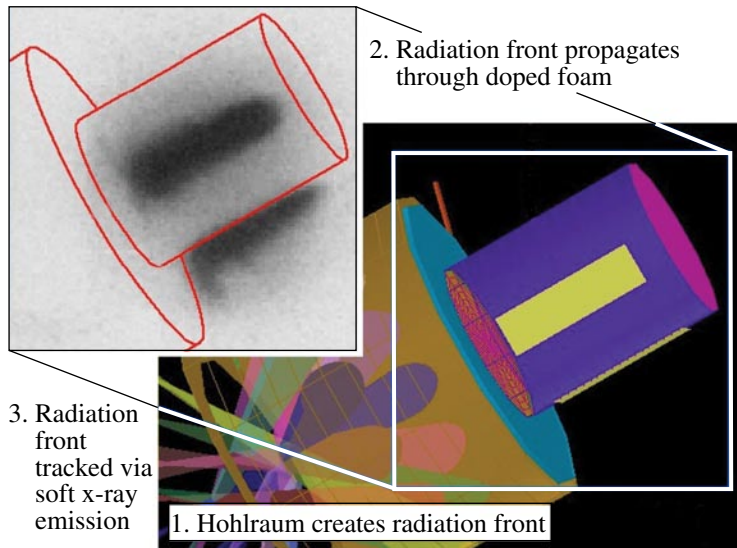   emission

1. Hohlraum creates radiation front

Figure 104.88
Sixteen beams heat a gold hohlraum, which produce a radiation front that propagates through the foam. Diagnostics slits allow measurement of the front's progression.
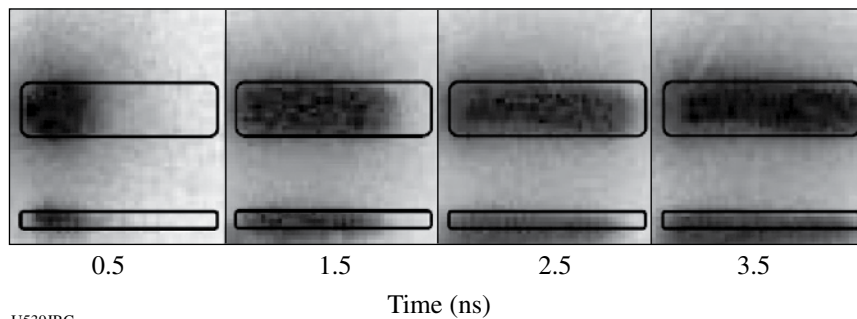

0.5   1.5   2.5   3.5

Time (ns)

U539JRC

Figure 104.89
The temporal evolution of the radiation front as tracked by the soft x-ray emission.

No Au

2-μm particles

0.5-μm particles

Intensity

0.5   1.0   1.5   2.0

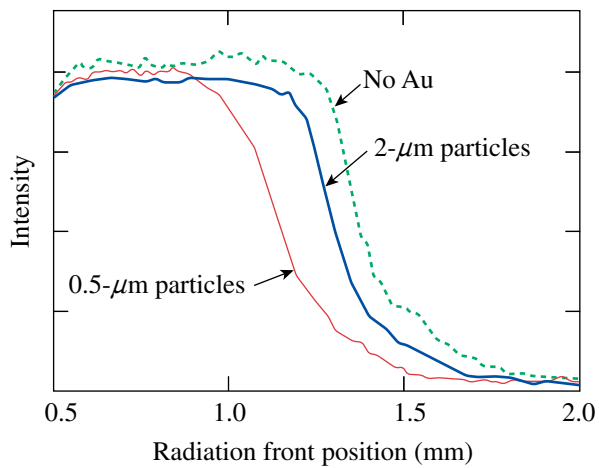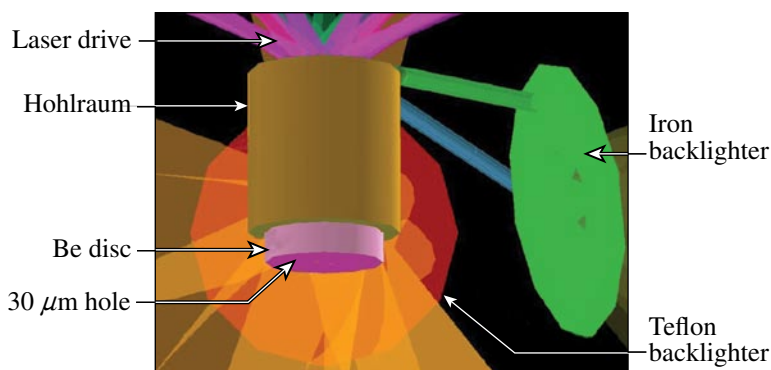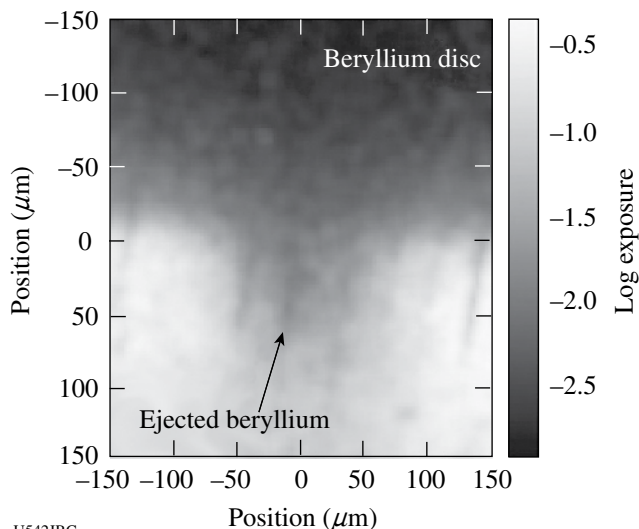Radiation front position (mm)

U540JRC

Figure 104.90
The radiation front position at 3.5 ns as it propagates through three foam types: no gold, 2-μm particles, and 0.5-μm particles. Data clearly show that propagation is slowed as gold particulates become smaller.

Laser drive
Hohlraum
Iron backlighter
Be disc
30 μm hole
Teflon backlighter

U541JRC

Figure 104.91
A heated gold hohlraum drives a shock into the beryllium disc creating a jet as the Be is forced out the small hole at the bottom. The Be jet and disc are imaged from two orthogonal directions.

Beryllium disc

Ejected beryllium

U542JRC

Figure 104.92
Radiograph from shot 40407 showing the jetting of copper-doped (0.9%) beryllium at 4 ns. The central photon energy was 310 eV (C He-α). The jet has expanded about 100 μm into the vacuum.

ACE-D: The ACE-D experiment on OMEGA investigated several areas of radiation hydrodynamics in preparation for experiments using two bundles of the NIF. One research avenue was to decrease the size of the hohlraums to create higher radiation temperatures. Using 3/4-scale hohlraums, radiation temperatures of higher than 220 eV were reached. A second test was to line the hohlraum with a low-density (9 mg/cm^3) aerogel foam to decrease the influx of Au wall material into the radiographic line of sight. The liner noticeably prevented the wall from occluding the line of sight, but the radiation temperature was also reduced substantially. There was, however, no increase in backscattered energy due to either stimulated Raman scattering (SRS) or stimulated brillouin scattering (SBS) as measured by the full-aperture backscatter (FABS) calorimeter.

Pinhole-Apertured, Point-Projection Backlighter (PAPBL) Studies: Imaging experiments at the NIF require the use of pinhole-apertured, point-projection backlighting (PAPBL) with gated instruments. Although this technique provides a much

more efficient use of backlighter photons, the absence of a pinhole array between the target and imaging system greatly enhances the susceptibility to extraneous noise sources. With this in mind, backlighter development experiments were performed at OMEGA to developed techniques to mitigate these undesired sources that degrade image quality.

The main objective of these experiments was to successfully image a driven hohlraum using zinc and germanium K-shell lines. The target consisted of a hohlraum with two gold grids mounted on the rear. Two orthogonal backlighters were used and a conical shield served to mitigate the noise source arising for the driven hohlraum (Fig. 104.93).

Images were obtained of the hohlraum's rear, including the grids for both undriven and driven hohlraums using a zinc backlighter. Moreover, we also obtained an undriven image of the hohlraum using a Ge (10.3 keV) backlighter (Fig. 104.94). This experiement's results provide confidence that orthogonal PAPBL imaging can be used successfully in the future.
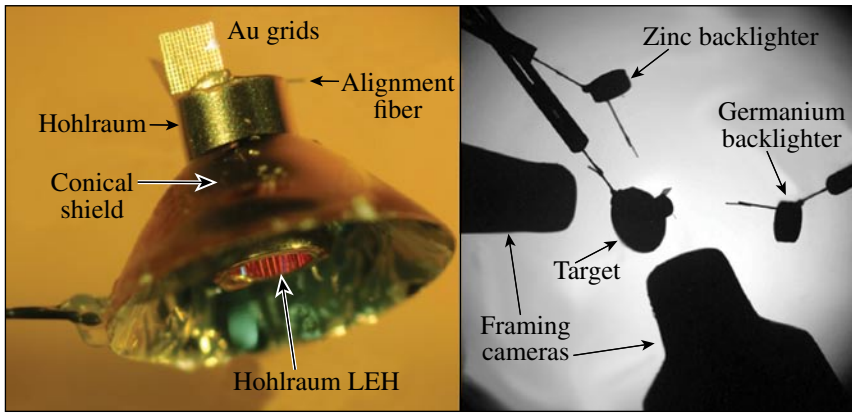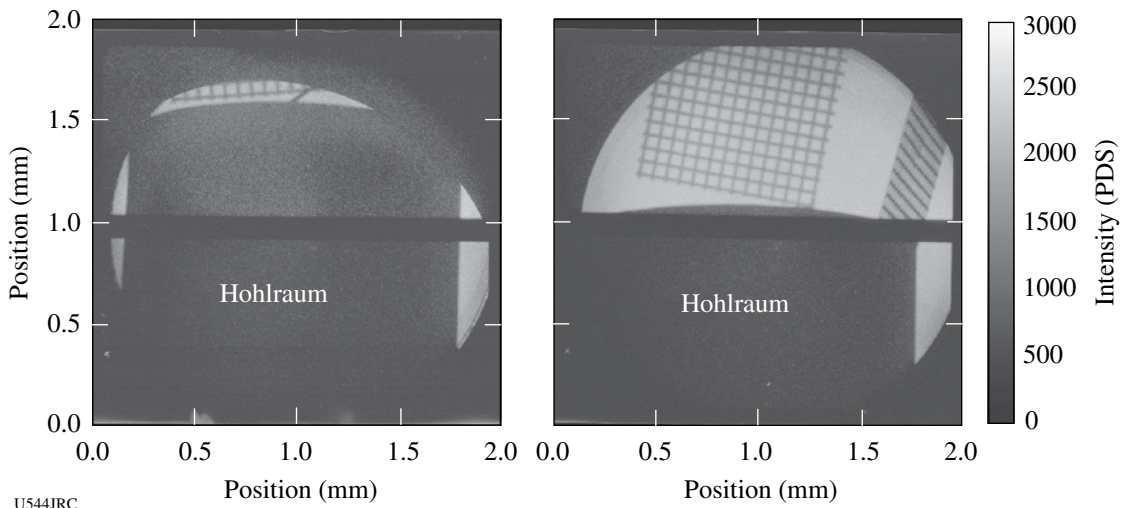
Figure 104.93

(a) An optical picture of the target showing the hohlraum, gold grids, and large gold conical shield. (b) The pre-shot target viewing system image of the experimental configuration showing the locations of the hohlraum, Zn and Ge backlighters, and two nose tips for the diagnostics.

Figure 104.94

(a) An image of a driven hohlraum with a Zn (~9 keV) backlighter. Some background noise from the driven hohlraum is still present, but the grid is still quite resolved. (b) An undriven hohlraum using a Ge backlighter (10.3 keV). As expected, the grids show very nice resolution.

High-Z Shell Implosions: Initial proof-of-principle experiments studying the effect of high-Z dopants on capsule burn were completed. These early experiments utilized deuterium-filled ignition capsules in which differing levels of krypton gas were introduced as a dopant. Previous experiments show that our hydrocodes calculate the effect of the high-Z dopant in ignition capsules poorly. Measurements of the neutron yield, ion temperature, and x-ray emission from the hot gas were obtained. Initial results indicate that the yield was lower than predicted, the ion temperature was higher than predicted, and the x-ray emission was lower than expected. More detailed analysis is being done to understand these results and to design FY06 experiments.

Time-Dependent Mix: The time-dependent mix campaign seeks to explore the mixing of shell material into the fuel of an inertial confinement fusion implosion. A thin layer of lightly doped titanium plastic is embedded into the inside surface of the plastic capsule. As the shell mixes into the fuel, the titanium heats up and radiates characteristic atomic lines that give information about the electron density and temperature in the vicinity of the titanium ions. The titanium was carefully chosen such that the ratio of more highly ionized to less ionized titanium could be used to infer the temperature at the point of emission, and thus tell us how far into the hot core the mix has reached at any particular time. The layer of titanium can be placed at the inside surface of the capsule or embedded

beneath the surface at a predefined depth. A series of capsules with progressively greater depths can tell us how much of the capsule material participates in mix. When the embedding depth is greater than the thickness of the layer that mixes, the hydrogenic titanium emission will disappear.

X-ray images of the capsule's implosion are shown in Fig. 104.95. The data clearly show the onset of K-shell emission arising from the titanium that has mixed into the core. We have determined that the amount of shell mix is between 0.5 and 1.0 μm and have also observed more mix than simulations would predict, thus constraining the parameters used in these models. This is apparent both from the nuclear yield and the amount of x-ray emission.
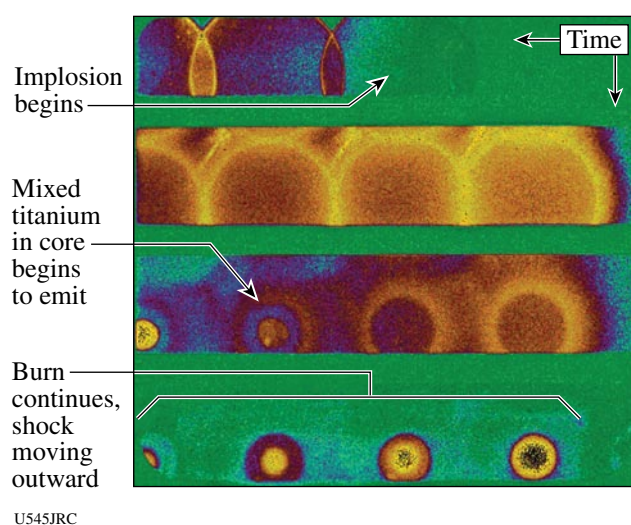

Figure 104.95
X-ray images of the capsule implosion showing the onset of titanium K-shell emission arising from the titanium that has mixed into the core.

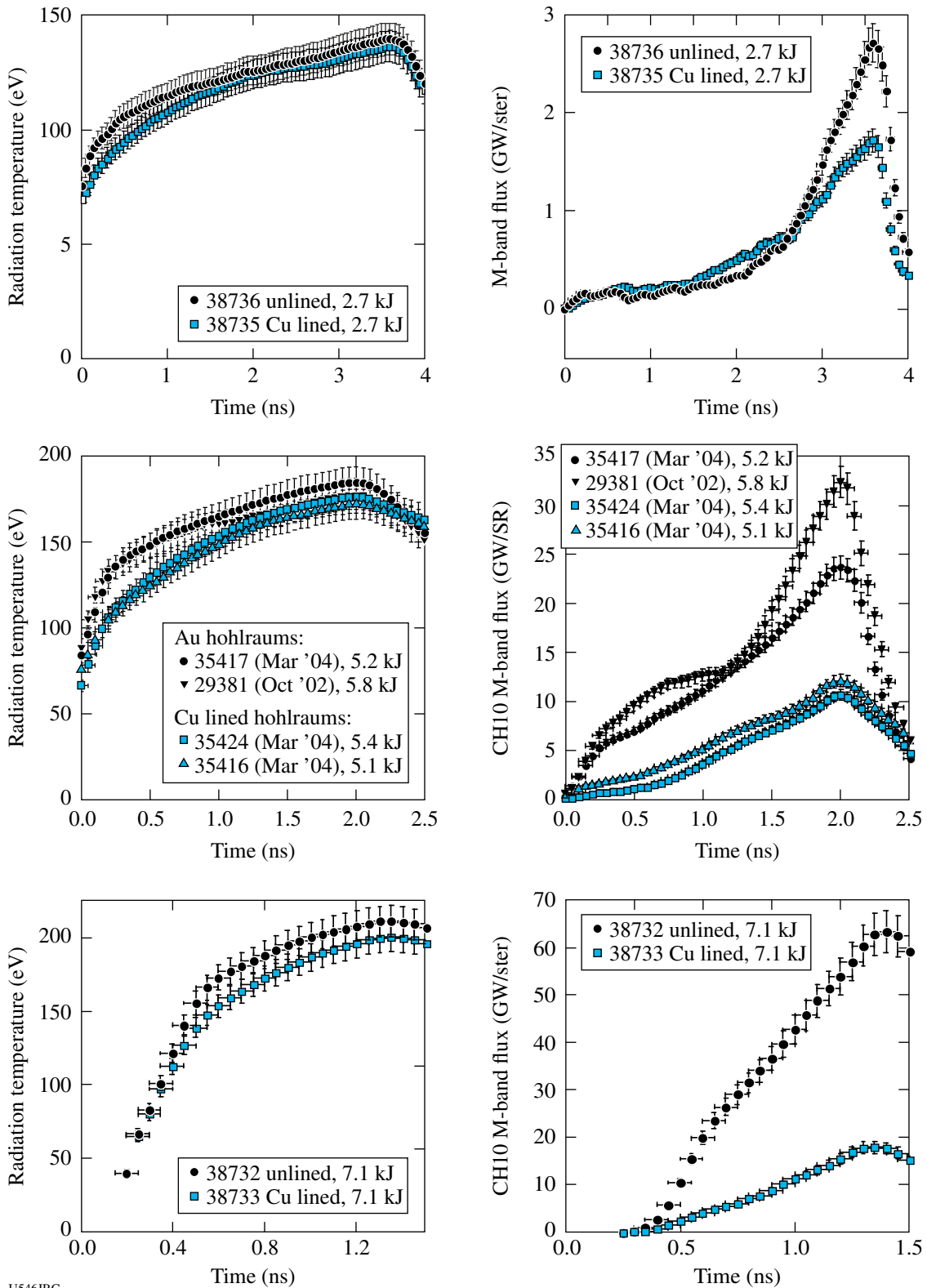## FY05 Sandia National Laboratories Experiments on OMEGA

SNL performed 31 target shots on OMEGA in FY05.

Modification of a Laser Hohlraum Spectrum via a Mid-Z Wall Liner: A typical laser hohlraum has a radiation spectrum that includes a significant component of non-Planckian, high-energy photons (such as Au M-band x rays) that originate in and near the hot, low-density coronal plasma in which the laser light is absorbed and converted into x-rays. These hard x-rays can have undesirable effects for an inertial confinement fusion (ICF) application, such as causing preheat ahead of the shock front in the ablator of an indirect-drive capsule.[5] In FY04 a

new concept was implemented for tailoring the spectrum in a hohlraum that uses a thin, mid-Z liner to supply plasma for the x-ray conversion with an underlying high-Z wall for x-ray containment.[6] In a series of FY05 experiments performed at the OMEGA Laser Facility, this concept was demonstrated to be effective for a wide range of laser intensities and hohlraum temperatures. The DANTE unfolded radiation temperature shown in Fig. 104.96 illustrate the dramatic reduction in M-band flux as the associated hohlraum temperatures increase over the range of 120 to 200 eV.
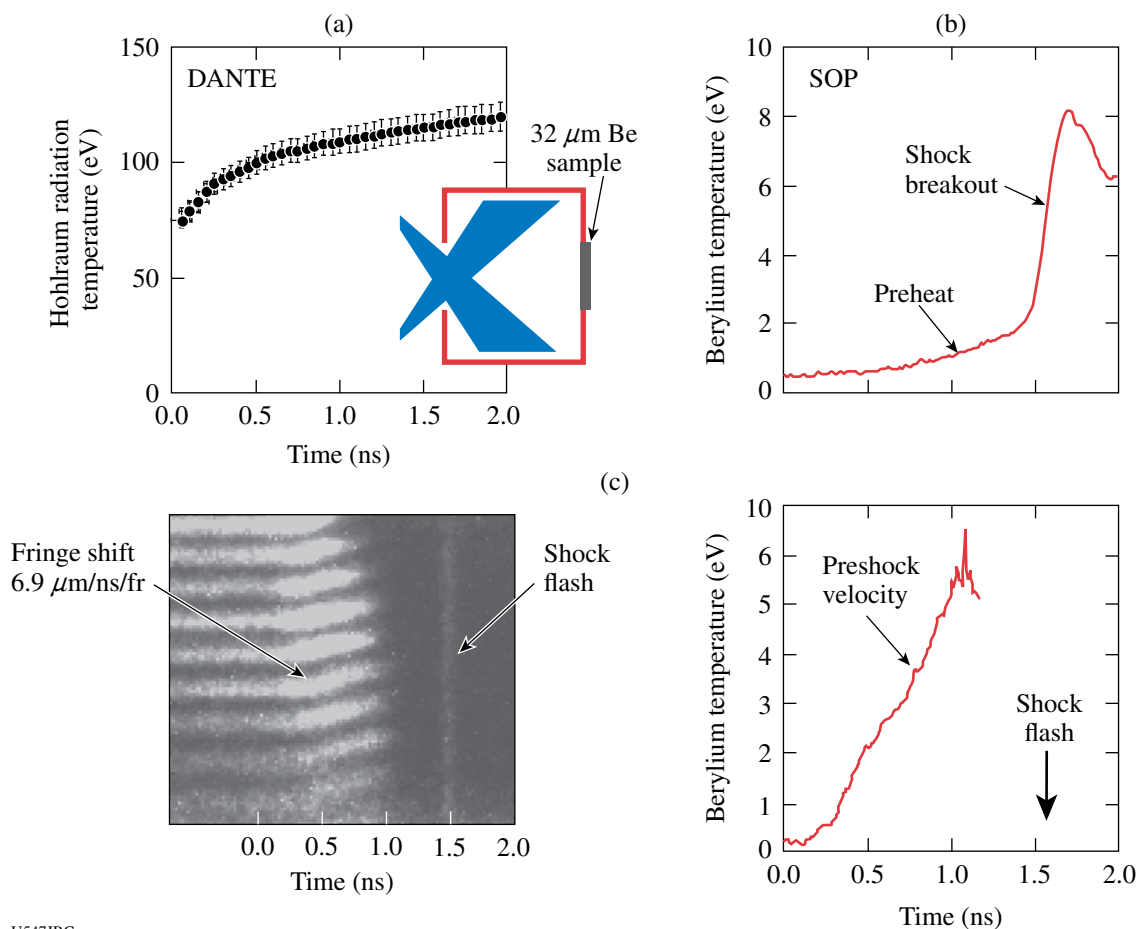
X-Ray Preheat in Indirect-Drive ICF Ablator Materials: In previous work[5] measurements of ablator shock velocities, shock temperatures, and preheat temperatures were made using a 280-nm streaked optical pyrometer (SOP).[7] More recent ablator experiments on OMEGA have extended this work by using an absolutely calibrated 600 to 800 nm SOP[8] with a line-imaging velocity interferometer.[9] Important new information has been obtained relating to ablator surface movement prior to shock breakout, ablator preheat temperature, and preheat effects on the anvil and window components of the shock-timing diagnostic system. Results from an experiment involving a 32-μm-thick beryllium ablator are shown in Fig. 104.97. In this experiment, 15 OMEGA beams delivered 2.8 kJ (in a 3.7-ns square pulse) into the interior of the hohlraum. The DANTE measurement of the hohlraum radiation temperature is shown in Fig. 104.97(a); the SOP measurement of the temperature of the exterior-facing side of the Be sample in Fig 104.97(b); and the VISAR measurement of the surface velocity of the Be sample in Fig 104.97(c). For all plots, time is relative to laser turn on at $t = 0$. Shock breakout occurs at ~1.5 ns with peak of the shock flash intensity occuring approximately 200 ps later. As indicated in Fig. 104.97(a), the hohlraum radiation temperature prior to $t = 1.5$ ns is in the range of 75 to 115 eV. Figure 104.97(b) indicates a pre-shock heating of the external Be surface to ~2 eV prior to shock breakout. Figure 104.97(d) indicates that the Be surface begins moving soon after the laser turn on and reaches a pre-shock velocity exceeding 6 μm/ns. As can be seen in Fig. 104.97(c), this velocity cannot measured for times >1.1 ns because of the loss of surface reflectivity. Per Fig. 104.97(b), the surface temperature at the time of reflectivity loss is approximately 1 eV.

Indirect-Drive ICF Shock Timing Diagnostic Development Experiments: Accurate measurements of shock timing and ablator x-ray burnthrough will be essential for the successful ignition of an indirect-drive ICF capsule. In FY05, we performed the initial tests of an experimental platform similar to the diagnostic proposed for accurate National Ignition Facility

Figure 104.96

DANTE-unfolded radiation temperature as a function of time for several hohlraum configurations (three plots on the left). M-band intensity versus time for the same shots (three plots on the right).

Figure 104.97
Indirect-drive experiment with a 32-mm-thick Be ablator. (a) DANTE measurement of hohlraum radiation temperature versus time, (b) SOP measurement of Be surface temperature versus time, (c) VISAR data showing fringe shift and shock flash, and (d) VISAR measurement of Be surface velocity.

(NIF) ignition shock-timing measurements.[10] Full-scale ignition capsules and pre-ignition shock-timing experiments at the NIF will utilize Cu-doped Be ablators with a thickness of ~150 μm. Our first attempts at testing the proposed shock-timing techniques utilized the geometry illustrated in Fig. 104.98. The 150-μm-thick ablator sample consisted of a pair of 75-μm-thick Be foils with a 0.5-μm-thick Cu foil sandwiched between the Be foils. In terms of overall ablator thickness and opacity, this approximates the proposed NIF ignition capsule ablator. A window was placed at a distance of ~1 mm from the ablator surface. In a few experiments, a liquid deuterium-filled cryostat was attached to the hohlraum, with the window at the same location (Fig. 104.99). Results from a experiment with a relatively low temperature hohlraum drive are shown in Fig. 104.98. In this experiment, the 15 OMEGA beams delivered 1.5 kJ (in a 3.7-ns square pulse) into the interior of the hohlraum. The DANTE measurement of hohlraum radiation

temperature is shown in Fig. 104.98(a), and the SOP measurement of the temperature of the exterior-facing side of the Be sample is shown in Fig. 104.98(b). As can be seen in the figure, the surface preheat begins soon after laser turn on and the surface temperature levels off at ~3.7 ns, when the laser turns off. Shock breakout occurs at ~7.2 ns. In relation to the experiment of Fig. 104.97, the reduced preheat level in Fig. 104.98 is consistent with the lower hohlraum temperature, the Cu component, and the thicker ablator. As explained in Ref. 5, the lower shock temperature is consistent with the reduced level of ablator preheat. An important finding in these experiments is that as hohlraum temperatures (and laser-spot intensities) are increased, the window is (apparently) also preheated and becomes opaque. A quartz window remained transparent throughout the laser pulse for hohlraumm temperatures of up to 136 eV [Fig. 104.99(a)]. For hohlraum temperatures exceeding 140 eV (corresponding to laser intensities at the hohlraum
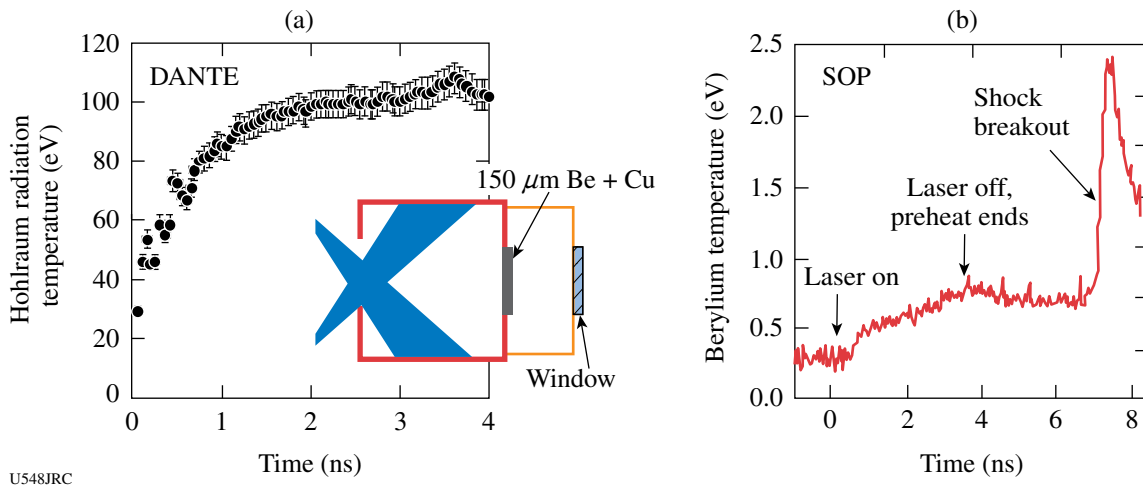
Figure 104.98
Shock breakout measurements: (a) DANTE-derived radiation temperature and (b) SOP-measured temperature of the exterior of the Be foil.
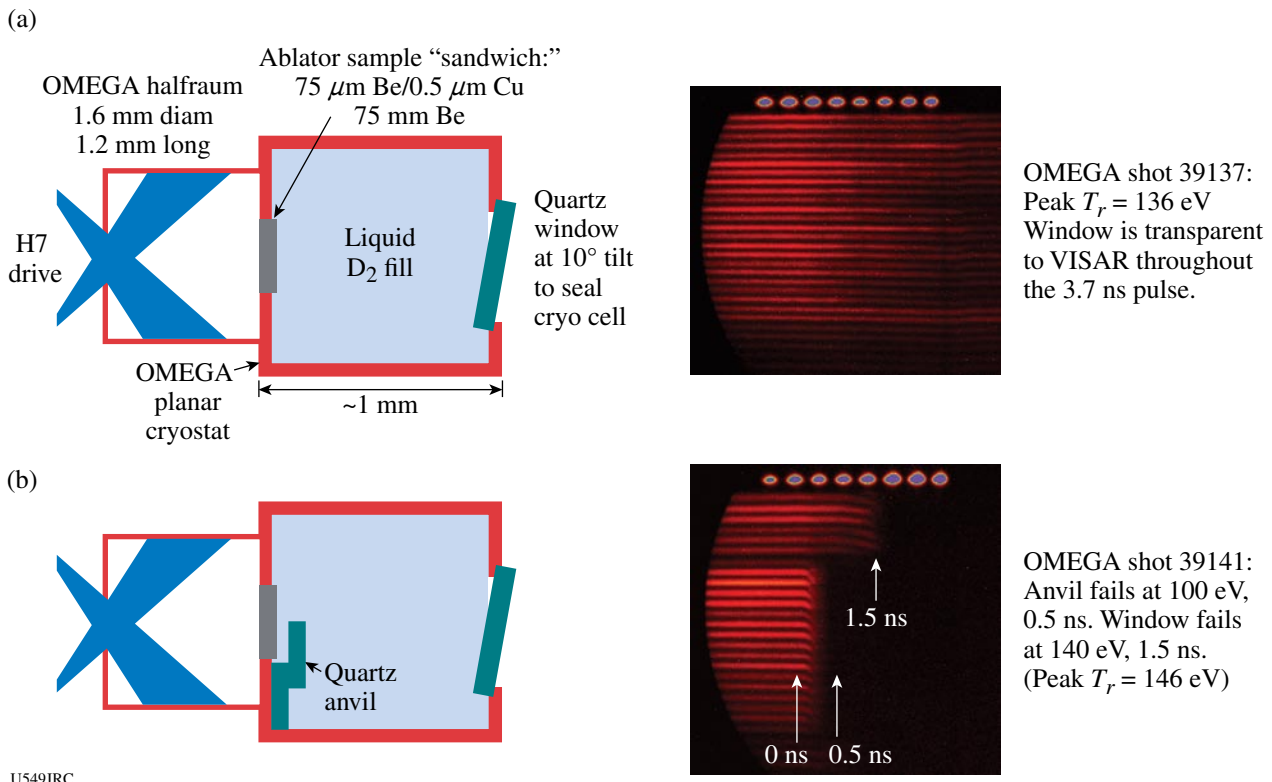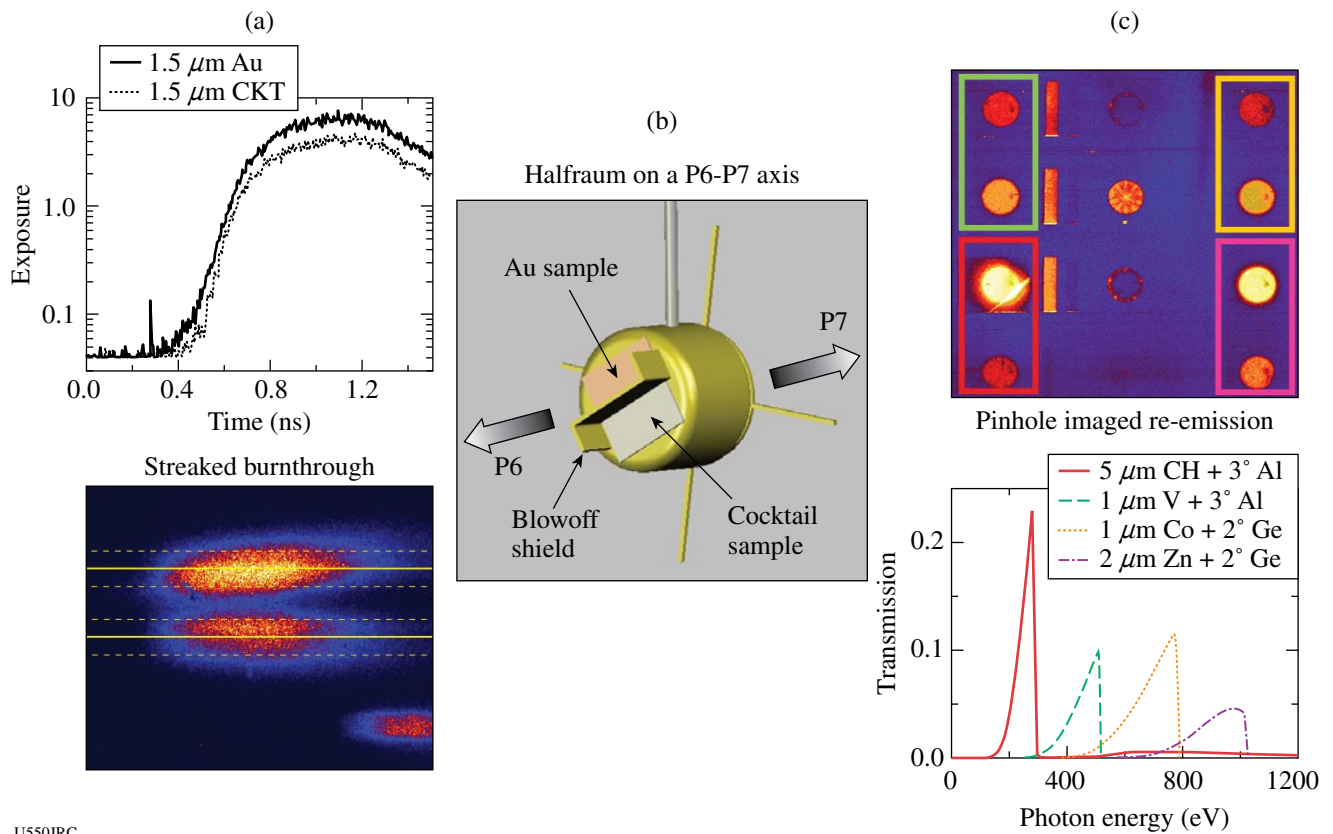

Figure 104.99
Window transparency: (a) quartz window maintains transparency up to $T_r \sim 136$ eV, (b) quartz anvil becomes opaque at $T_r > 100$ eV and window fails at 140 eV.

wall ~1 × 10^14 W/cm²), however, windows and anvils became opaque soon after laser turn on [Fig. 104.99(b)]. In the near future, new window materials, laser smoothing, and geometric effects will be tested in an attempt to reduce window and anvil preheat effects to a level consistent with the requirements of the proposed NIF shock-timing diagnostic.

Cocktail Burnthrough and Re-emission: SNL conducted 11 shots in June 2005 to study the relative difference in burn-through time and x-ray re-emission between thin cocktail and Au foils. Figure 104.100 shows the sample geometry and example data for the experiments. These were the first tests of the layered 75% U, 25% Au cocktail material made by General Atomics that is currently specified as the hohlraum wall material in the NIF point design. The experiments studied the difference in performance between cocktails and Au in hohl-

raums with peak radiation temperatures of 175 eV, 235 eV, and 270 eV. Preliminary results show that the difference in burn-through between Au and cocktails at 550-eV photon energy is ~0 ps at T_r = 170 eV, and ~50 ps at T_r = 230 eV (the foils in the 270-eV hohlraums burnthrough at a time when the radiation temperature is ~230 eV). Time-gated x-ray pinhole camera measurements were configured with four different filter-mirror combinations to sample the wall re-emission across spectral ranges of ~200 to 250 eV, ~400 to 500 eV, ~600 to 800 eV, and ~800 to 1000 eV. Preliminary results show a 20±15% increase in the re-emission from cocktails in the energy band from ~400 to 500 eV at hohlraum radiation temperatures >220 eV and no statistically significant increase or decrease in any other energy band. Future work will include detailed comparisons between the experimental data and integrated *LASNEX* calculations with the best known opacities of Au and U.

U550JRC

Figure 104.100
Example data, (a) and (c), and geometry (b) from cocktail burnthrough and re-emission experiments conducted by SNL in June 2005. On the left is burnthrough data (b) taken with an x-ray streak camera at P6, and on the right (c) is x-ray framing camera data at P7 with four different mirrored channels.

2005 CEA Experiments on OMEGA

Scientists from CEA led several OMEGA experimental campaigns in FY05 including the development of neutron imaging and hohlraum symmetry experiments. A total of 34 OMEGA target shots were taken for CEA experiments in FY05.

Penumbral and Annular Imaging for Inertial Confinement Fusion Neutron Images

1. Introduction

In inertial confinement fusion experiments, laser energy is used to compress a millimeter-sized (diameter) target filled with deuterium and tritium. The compression results in the creation of a hot spot where the fusion reactions begin. On the NIF (U.S.A.) or LMJ (France), 14-MeV neutron images will be used to determine the dimensions and the shape of the hot spot. Since the dimensions of the hot spot will be ~50 μm, a spatial resolution below 10 μm will be required in a neutron image to distinguish between the different failure mechanisms of the implosion (symmetry, laser pulse shaping, etc.).

CEA developed a neutron imaging system (NIS) using a penumbral[11,12] and, most recently, an annular[13] imaging technique with a high-resolution neutron camera that was tested on OMEGA during high-neutron-yield shots. The images obtained with these tests attained a 20-μm spatial resolution with a high signal-to-noise ratio (SNR). With these results we can now consider a preliminary design for a NIS with a resolution of 10 μm on OMEGA and 6 to 7 μm on the NIF or LMJ.

2. Experimental Setup

Neutrons emitted by the target go through a coded aperture that is placed 26 cm from target chamber center (TCC). Two coded apertures can be used: a penumbral or an annular. Both are made of a biconical hole built in a 10-cm-long DENAL (Tungsten alloy) cylinder. The diameter at the intersection of the cones is ~2 mm. The ring is obtained by placing a plug inside the hole so that the aperture is equivalent to a continuous assembly of 8-μm-diam pinholes distributed along a circle (Fig. 104.101).

An enlarged image of the coded aperture is projected on a neutron camera placed at a distance of ~8 m from TCC. The camera is composed of a coherent array of one-million glass capillaries, 85 μm in diameter, filled with a high-refractive-index organic liquid scintillator. Neutrons mainly interact by elastic scattering on hydrogen nuclei. As they lose kinetic energy, the recoil protons produce light, a part of which is guided through the stepped-index fiber optics made by glass

($n = 1.49$) and scintillator ($n = 1.56$). The image is then transported, intensified, and reduced to be registered on a one-million pixel CCD (20×20 mm^2).

The spatial resolution Δs of the overall system is given by

$$\Delta s = \sqrt{\left[\frac{\ln(2) \times FOV}{2 \times L_0 \times \mu}\right]^2 + \Delta s_{det}^2 \times \left(\frac{L_0}{L_1}\right)^2} \, , \qquad (1)$$

where FOV is the field of view, L_0 and L_1 the target to aperture and target to detector distances, respectively, Δs_{det} is the resolution of the camera, and μ is the attenuation of neutrons in the DENAL cylinder. During the past few years, improvements in the detector design have led to the achievement of a camera resolution of ~650-μm FWHM. Since the camera resolution is limited primarily by the recoil length of protons, this value can be reduced to 400 μm by replacing hydrogen atoms with deuterium in the scintillator.[14]

Penumbral aperture

100 mm

1.7 mm

2.057 mm

2.491 mm

Annual aperture

1.7 mm

1.623 mm
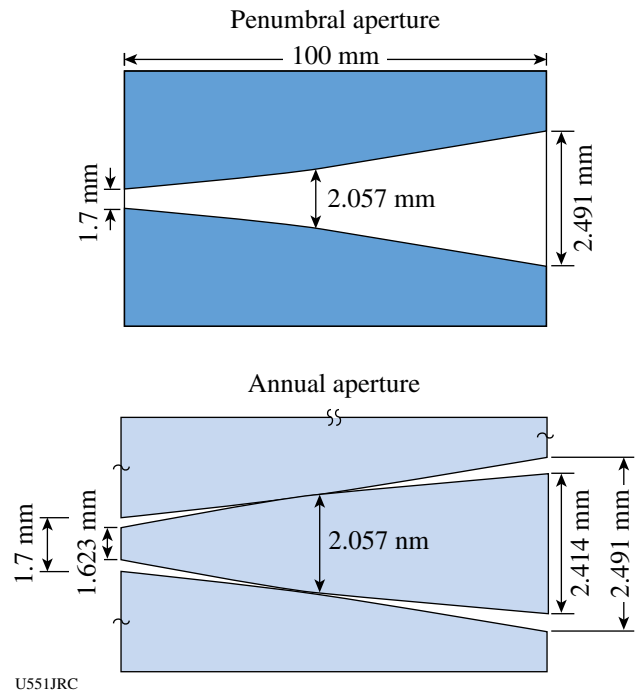
2.057 nm

2.414 mm

2.491 mm

U551JRC

Figure 104.101

Sections of the penumbral- and annular-coded apertures. Both have the same dimensions. A plug is placed inside the second aperture to define a ring equivalent aperture.

3. 2005 High-Yield Shots

In 2004, neutron images were acquired with the penumbral technique. A spatial resolution of 20 μm and a SNR of ~20 to 25 were demonstrated with this system. In 2005, the detector was unchanged except for replacement of the fiber optic reducer (taper) between the capillary array and the microchannel plate (MCP). The quality of this taper improved the uniformity and the transmission of the image on the whole field of view. The annular imaging technique was tested and compared with results obtained with the penumbral aperture for the same type of targets to prove the reliability of the technique. Figure 104.102 presents raw images, penumbral and annular, for plastic-shell targets and compares annular images for a plastic and a glass target. Glass targets produce a larger core than plastic ones. This is confirmed by observing the raw images as the thickness of the ring is directly related to the source diameter in one dimension. Figure 104.103 shows unfolded images for both techniques on DT(15)CH[15], DT(15)CH[20], and DT(15)SiO$_2$[2.5] targets. The images have a 20-μm spatial resolution. The corresponding neutron yields Y_n and SNR are written on each image. Plastic targets have a high convergence ratio for relatively high yields, which leads to very good SNR around 30 to 40. Though glass targets result in higher neutron yields, the larger cores produce images with a lower SNR of ~15. Comparison of the penumbral and annular images shows that the dimensions and shape of the hot-spot dimensions are the same for similar targets. The ring technique was chosen because it will result in a high SNR in high-resolution images. This was confirmed by applying a 20-μm and then a 10-μm FWHM low-pass filter on the image for both techniques. The SNR of both penumbral and annular images was near 40 for a 20-μm filter, though it decreased to 14 in the penumbral image and still remained 28 in the ring image for a 10-μm filter.[15]
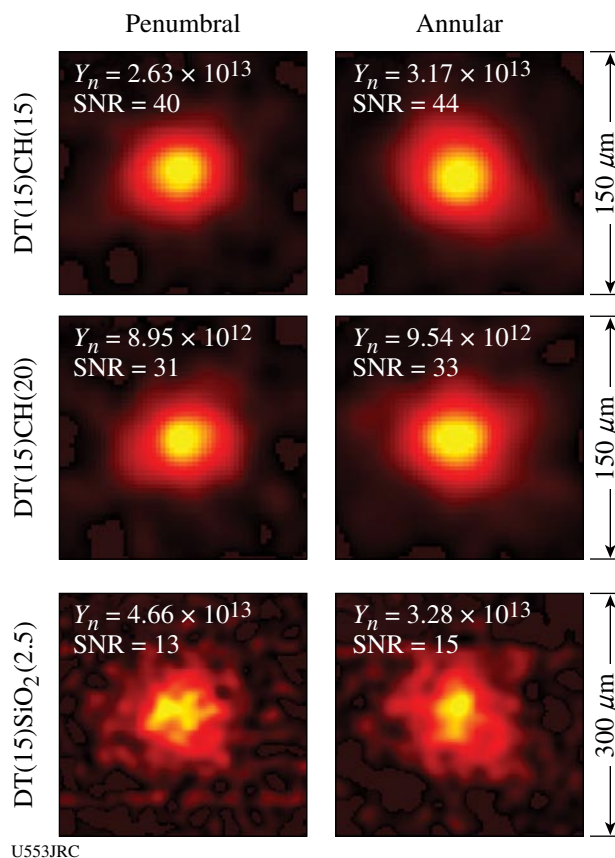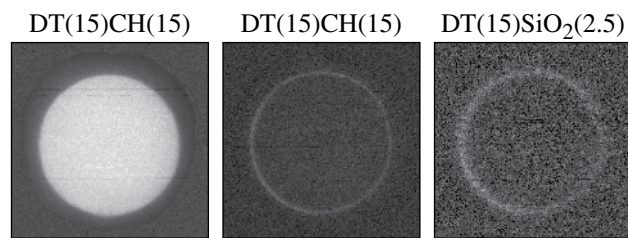

Figure 104.103
Unfolded images obtained during 2005 high-yield shots. Comparison between penumbral and annular techniques for three types of targets.

Figure 104.102
Raw images obtained with a penumbral (left) and an annular (center and right) apertures.

4. 2005 DD Shots

With 2.45-MeV DD neutrons, the recoil ion length in the scintillator is much shorter. As a consequence, the resolution of the detector is much better, ~230 μm compared to ~650 μm for DT neutrons. The improved sensitivity of the camera is sufficient to acquire a DD image with a neutron yield of about 10^{11}. Neutron images were thus registered on DD shots, including cryogenic targets. Figure 104.104 shows examples of neutron images obtained with a cryogenic target (left) and with a gas-filled plastic shell target (right). The resolution is set to 50 μm and 35 μm, respectively, because of the low yield relatively close to the threshold of sensitivity of the camera, which implies a compromise between resolution and SNR.
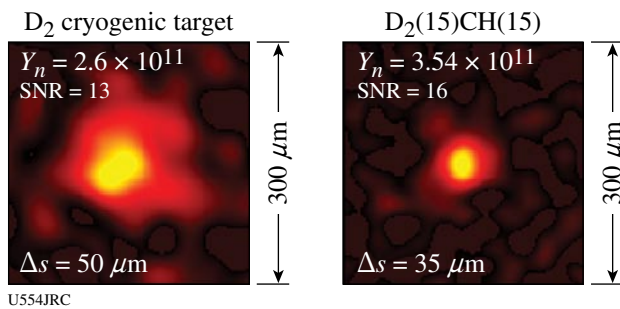

U554JRC

Figure 104.104
Neutron images of DD targets.

5. Conclusions

During the 2005 high-yield shots on OMEGA, DT neutron images were acquired with a 20-μm spatial resolution and very high SNR. The annular imaging technique was tested and demonstrated higher signal-to-noise ratio images compared to the penumbral imaging technique. With an enhanced detector and a ring-coded aperture, a 10-μm spatial resolution on OMEGA and 10-μm spatial resolution on the NIF or LMJ is now projected.
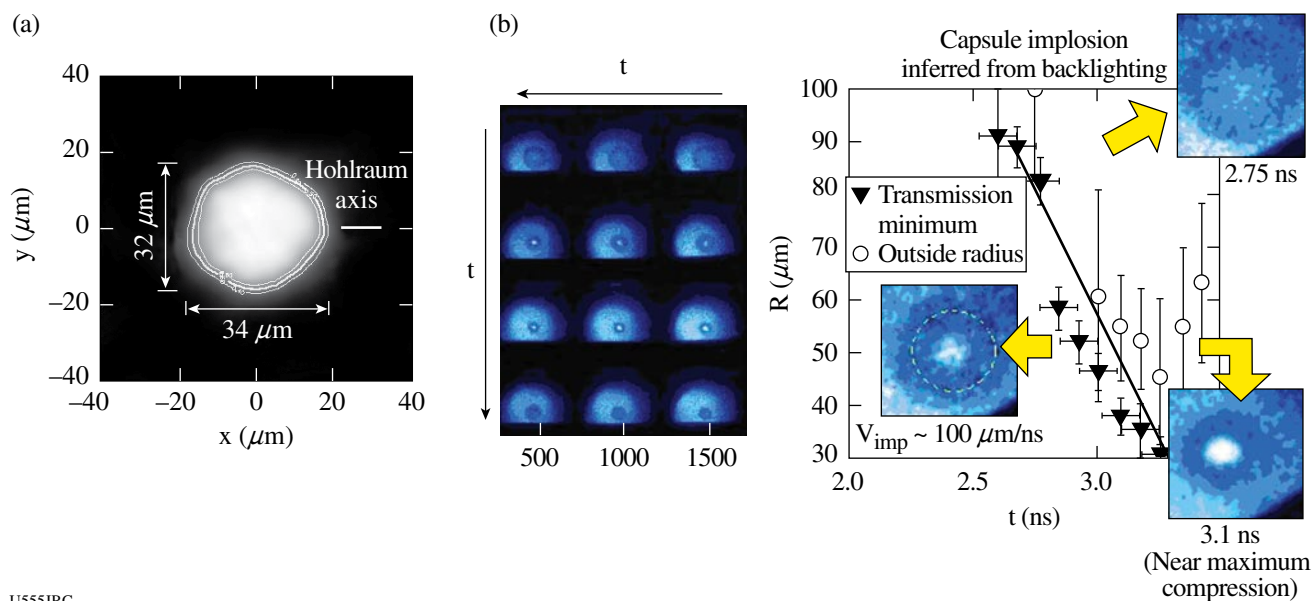
The neutron camera was sensitive enough to acquire DD images, but the low yield resulted in a reduction to the resolution to improve the quality of the image. A new detector design is now being considered to acquire DD neutron images. This camera will have an enhanced detection quantum efficiency with smaller dimensions to work with a lower magnification ratio.

CEA Symmetry Experiments

In previous years, CEA carried out an experimental campaign to study the irradiation symmetry of radiation-driven capsules in cylindrical hohlraums heated by a multicone arrangement of beams. In FY05, CEA experiments were carried out to characterize the symmetry by imaging the core x-ray emission[16] of 500-μm, 50-atm, D_2-filled capsules doped with 0.1-atm argon. These capsules were produced by CEA/Valduc. Shell thickness variation was used to probe symmetry at different times during the implosion.

Figure 104.105(a) gives an example of a core image obtained with a 37-μm CH, 2% at., Ge-doped capsule. This image is obtained at an instant (3.1 ns) close to peak compression. The convergence ratio Cr ~ 7 can be determined on a similar capsule by backlighting the shell implosion. From Cr and core ellipticity, we can infer an irradiation P2 component of ~1% (Ref. 17), which is consistent with the expected symmetry from previous foam-ball experimental data, time-integrated evolution of flux P2 component in simulations, and also with data reported in Ref. 18.

Backlighting tests of imploding capsules were carried out. Figure 104.105(b) shows an example of a shot where a simultaneous image of core emission and backlighting of the dense shell is recorded. This provides valuable data to benchmark hydrodynamic simulations. We can infer from these data an implosion velocity of ~100 μm/ns and a convergence ratio from the minimum radius of the dense part of the shell of ~7.

U555JRC

Figure 104.105
(a) Example of an imploded core image. (b) Backlit image of imploding capsule showing, on the same data, an image of core emission and absorption through the dense part of the shell.

REFERENCES

1. S. D. Rothman *et al.*, J. Phys. D **38**, 733 (2005).

2. W. J. Nellis *et al.*, Phys. Rev. Lett. **53**, 1248 (1998).

3. V. Ya. Ternovoi *et al.*, in *Shock Compression of Condensed Matter, AIP Conference Proceedings 620*, edited by M. D. Furnish, N. N. Thadhani, and Y. Horie (American Institute of Physics, New York, 2002), pp. 107–110.

4. A. Forster, T. Kahlbaum, and W. Ebeling, Laser Part. Beams **10**, 253 (1992).

5. R. E. Olson *et al.*, Phys. Rev. Lett. **91**, 235002 (2003).

6. R. E. Olson *et al.*, Bull. Am. Phys. Soc. **49**, 24 (2004).

7. J. A. Oertel *et al.*, Rev. Sci. Instrum. **70**, 803 (1999).

8. J. Miller, T. R. Boehly, E. Vianello, W. J. Armstrong, C. Sorce, W. Theobald, D. D. Meyerhofer, J. Eggert, and D. G. Hicks, Bull. Am. Phys. Soc. **49**, 64 (2004).

9. P. M. Celliers, D. K. Bradley, G. W. Collins, D. G. Hicks, T. R. Boehly, and W. J. Armstrong, Rev. Sci. Instrum. **75**, 4916 (2004).

10. D. H. Munro *et al.*, Phys. Plasmas **8**, 2245 (2001).

11. A. Rouyer, Rev. Sci. Instrum. **74**, 1234 (2003).

12. R. A. Lerche *et al.*, Laser Part. Beams **9**, 99 (1991).

13. R. G. Simpson *et al.*, Opt. Eng. **14**, 490 (1975).

14. L. Disdier, R. A. Lerche, J. L. Bourgade, and V. Yu. Glebov, Rev. Sci. Instrum. **75**, 2134 (2004).

15. L. Disdier, A. Rouyer, I. Lantuejoul, O. Landuas, J. L. Bourgade, T. C. Sangster, V. Yu. Glebov, and R. A. Lerche, "Inertial Confinement Fusion Neutron Images," to be published in Physics of Plasma.

16. A. Hauer *et al.*, Rev. Sci. Instrum. **66**, 672 (1995).

17. J. D. Lindl *et al.*, Phys. Plasmas **11**, 339 (2004).

18. P. Amendt, R. E. Turner, and O. L. Landen, Phys. Rev. Lett. **89**, 165001 (2002).